Nano Research

ISSN 1998-0124 CN 11-5974/O4
https://doi.org/10.1007/s12274-024-6460-5

Research Article

Ruthenium-lead oxide for acidic oxygen evolution reaction in proton exchange membrane water electrolysis

Feng-Yang Chen[1,†], Chang Qiu[1,†], Zhen-Yu Wu[1,†], Tae-Ung Wi[1], Y. Zou Finfrock[2], Haotian Wang[1,3,4](✉)

[1] Department of Chemical and Biomolecular Engineering, Rice University, Houston, TX 77005, USA

[2] Structural Biology Center, X-ray Science Division, Argonne National Laboratory, Lemont, IL 60439, USA

[3] Department of Materials Science and NanoEngineering, Rice University, Houston, TX 77005, USA

[4] Department of Chemistry, Rice University, Houston, TX 77005, USA

[†] These authors contributed equally to this work.

Nano Res., **Just Accepted Manuscript** • https://doi.org/10.1007/s12274-024-6460-5

http://www.thenanoresearch.com on Jan. 2, 2024

Just Accepted

Template for Preparation of Manuscripts for *Nano Research*

This template is to be used for preparing manuscripts for submission to *Nano Research*. Use of this template will save time in the review and production processes and will expedite publication. However, use of the template is not a requirement of submission. Do not modify the template in any way (delete spaces, modify font size/line height, etc.). If you need more detailed information about the preparation and submission of a manuscript to *Nano Research*, please see the latest version of the Instructions for Authors at http://www.thenanoresearch.com/.

TABLE OF CONTENTS (TOC)

Authors are required to submit a graphic entry for the Table of Contents (TOC) in conjunction with the manuscript title. This graphic should capture the readers' attention and give readers a visual impression of the essence of the paper. Labels, formulae, or numbers within the graphic must be legible at publication size. Tables or spectra are not acceptable. Color graphics are highly encouraged. The resolution of the figure should be at least 600 dpi. The size should be at least 50 mm × 80 mm with a rectangular shape (ideally, the ratio of height to width should be less than 1 and larger than 5/8). One to two sentences should be written below the figure to summarize the paper. To create the TOC, please insert your image in the template box below. Fonts, size, and spaces should not be changed.

Ruthenium-Lead Oxide for Acidic Oxygen Evolution Reaction in Proton Exchange Membrane Water Electrolysis

Feng-Yang Chen, Chang Qiu, Zhen-Yu Wu, Tae-Ung Wi, Y. Zou Finfrock, and Haotian Wang*

Rice University, USA
Argonne National Laboratory, USA

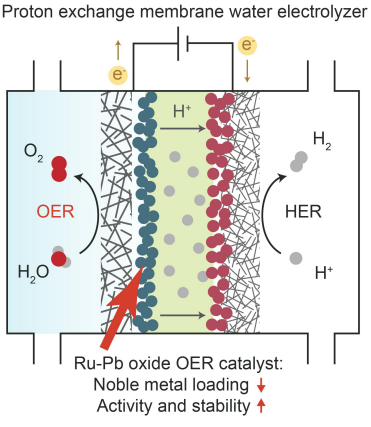

We design a Ru-based OER catalyst incorporating Pb as a supporting element, lowering the Ru noble metal loading while delivering a better activity and stability, maintaining up to 300 h of stability in a proton exchange membrane water electrolyzer.

Nano Research

ISSN 1998-0124 CN 11-5974/O4
https://doi.org/(automatically inserted by the publisher)

Ruthenium-lead oxide for acidic oxygen evolution reaction in proton exchange membrane water electrolysis

Feng-Yang Chen[1†], Chang Qiu[1†], Zhen-Yu Wu[1†], Tae-Ung Wi[1], Y. Zou Finfrock[2], and Haotian Wang[1,3,4](✉)

[1] *Department of Chemical and Biomolecular Engineering, Rice University, Houston, TX 77005, USA*
[2] *Structural Biology Center, X-ray Science Division, Argonne National Laboratory, Lemont, IL 60439, USA*
[3] *Department of Materials Science and NanoEngineering, Rice University, Houston, TX 77005, USA*
[4] *Department of Chemistry, Rice University, Houston, TX 77005, USA*
[†] *These authors contributed equally to this work*

Received: day month year / **Revised:** day month year / **Accepted:** day month year (automatically inserted by the publisher)

ABSTRACT

Developing an active and stable anode catalyst for the proton exchange membrane water electrolyzer (PEM-WE) is a critical objective to enhance the economic viability of green hydrogen technology. However, the expensive Iridium-based electrocatalyst remains the sole practical material with industrial-level stability for the acidic oxygen evolution reaction (OER) at the anode. Ruthenium-based catalysts have been proposed as more cost-effective alternatives with improved activity, though their stability requires enhancement. The current urgent goal is to reduce costs and noble metal loading of the OER catalyst while maintaining robust activity and stability. In this study, we design a Ru-based OER catalyst incorporating Pb as a supporting element. This electrocatalyst exhibits an OER overpotential of 201 mV at 10 mA cm^{-2}, simultaneously reducing Ru noble metal loading by ~40%. Normalization of the electrochemically active surface area unveils improved intrinsic activity compared to the pristine RuO_2 catalyst. During a practical stability test in a PEM-WE setup, our developed catalyst sustains stable performance over 300 h without notable degradation, underscoring its potential for future applications as a reliable anodic catalyst.

KEYWORDS

Electrocatalysis, Oxygen evolution reaction, Water splitting, Proton exchange membrane water electrolyzer

Introduction

Green hydrogen (H_2), produced via water electrolysis ($2H_2O \rightarrow 2H_2 + O_2$) using renewable electricity from sources like solar or wind, is widely regarded as one of the most pivotal fuels or chemicals for reshaping the energy landscape towards a sustainable future [1-4]. To date, conventional alkaline water electrolyzers (AWE) have maintained their dominance due to their independence from costly noble-metal catalysts [5, 6]. However, AWE encounters challenges, including high ohmic resistance, crossover of product gases, and a less compact design, that have constrained its potential for broad adoption in future applications of green hydrogen production [7, 8]. The proton exchange membrane water electrolyzer (PEM-WE), employing a polymer-based proton exchange membrane (PEM) as an ion conductor instead of liquid electrolyte, has arisen to address the aforementioned challenges, offering improved energy efficiency and attracting significant attention [9-11]. Nevertheless, the anode electrocatalyst in PEM-WE suffers from the extreme local acidic environment on the membrane. This harsh condition results in severe catalyst degradation, particularly during the anodic oxygen evolution reaction (OER) [12-15]. To address this challenge, designing an active, durable, and low-cost electrocatalyst for acidic OER is an indispensable mission for industrialization of PEM-WE for future green hydrogen generation.

Unfortunately, as of today, the options for OER catalysts demonstrating satisfactory stability remain severely limited. Currently, catalysts based on iridium (Ir), a costly noble-metal, stand as the only catalysts that have showcased industrial-level durability within PEM-WE devices [10, 11, 16, 17]. The scarcity and elevated cost (~ \$150 g^{-1}) of Ir impede the development of PEM-WE technology and represent a main obstacle to reducing the price

Address correspondence to Haotian Wang, htwang@rice.edu

of green hydrogen production [8, 14]. Ruthenium (Ru) based catalysts have been regarded as a promising alternative [18-20]. In comparison to Ir-based catalysts, Ru-based catalysts typically exhibit superior activity (overpotential < 300 mV), and Ruthenium costs less (~ \$20 g^{-1}) compared to Ir [18, 21-23]. Most notably, various studies have demonstrated stability lasting hundreds of hours for several Ru-based OER catalysts [24-28]. Although this is still far from meeting the requirements for industrial long-term stability, when compared to other transition metal oxides that mostly dissolve within ten hours under harsh acidic conditions, Ru stands out as an element with significant potential [18, 22, 29].

Despite being more affordable than the state-of-the-art commercial IrO_2 catalysts, Ru is still regarded as a costly noble metal. Therefore, lowering the loading of noble metals in OER catalysts for PEM-WE while maintaining similar activity and stability poses an urgent challenge that remains to be addressed. To achieve this goal, we demonstrate a strategy by introducing lead (Pb) as a supportive metal to synthesize a bimetallic Ru-Pb oxide. Previously, Pb-based catalysts have demonstrated decent stability under acidic conditions, although they do not exhibit outstanding OER activity [30, 31]. With this concept in mind, we observed in this study that Pb oxide can act as a supportive material for the RuO_2 active site. This allowed us to reduce the noble metal loading of Ru in the catalyst by ~40%, while simultaneously achieving improved OER activity (overpotential of 201 mV at 10 mA cm^{-2}). Electrochemically active surface area (ECSA) analysis revealed that this Ru-Pb oxide catalyst possesses a surface area similar to that of the RuO_2 nanoparticle control sample we synthesized, yet displays enhanced intrinsic activity. Most significantly, the Ru-Pb oxide exhibited great OER stability, withstanding over 3 days of testing using lab-scale rotating disk electrode (RDE) and enduring for more than 300 hours in a practical PEM-WE device without significant degradation.

Results

Synthesis and characterizations of catalysts. In this study, we introduced a systematic process for synthesizing a range of Ru-Pb oxide nanoparticles as OER catalysts (see Methods). Initially, a wet impregnation was conducted to uniformly mix the $RuCl_3$ and $PbNO_3$ precursors at the desired metal ratio on a carbon black support. Subsequently, the mixture underwent a two-step annealing process. The first step involved reduction through annealing under an H_2/Ar environment, followed by the second step of oxidation in air. This second step served to remove the carbon black support and oxide the metallic Ru and Pb into oxide forms. To optimize the Ru loading and catalyst activity, we synthesized various ratios of Ru-Pb oxide catalysts and assessed their performance using RDE. We observed that an atomic ratio of 3:1 of Ru to Pb (denoted as Ru_3PbOx) in this system yielded the best onset potential and nearly the lowest charge transfer resistance compared to other ratios (Fig. S1 in the Electronic Supplementary Material (ESM)). It's important to note that this 3:1 atomic ratio corresponds to a mass ratio of around 6:4. This suggests that if the same mass of Ru_3PbOx and RuO_2 is used as OER catalyst, the Ru loading is reduced by ~40%. Next, we pursued further optimization of the synthetic process by varying the annealing temperature in an air environment since this step is crucial, as it is the critical step that can

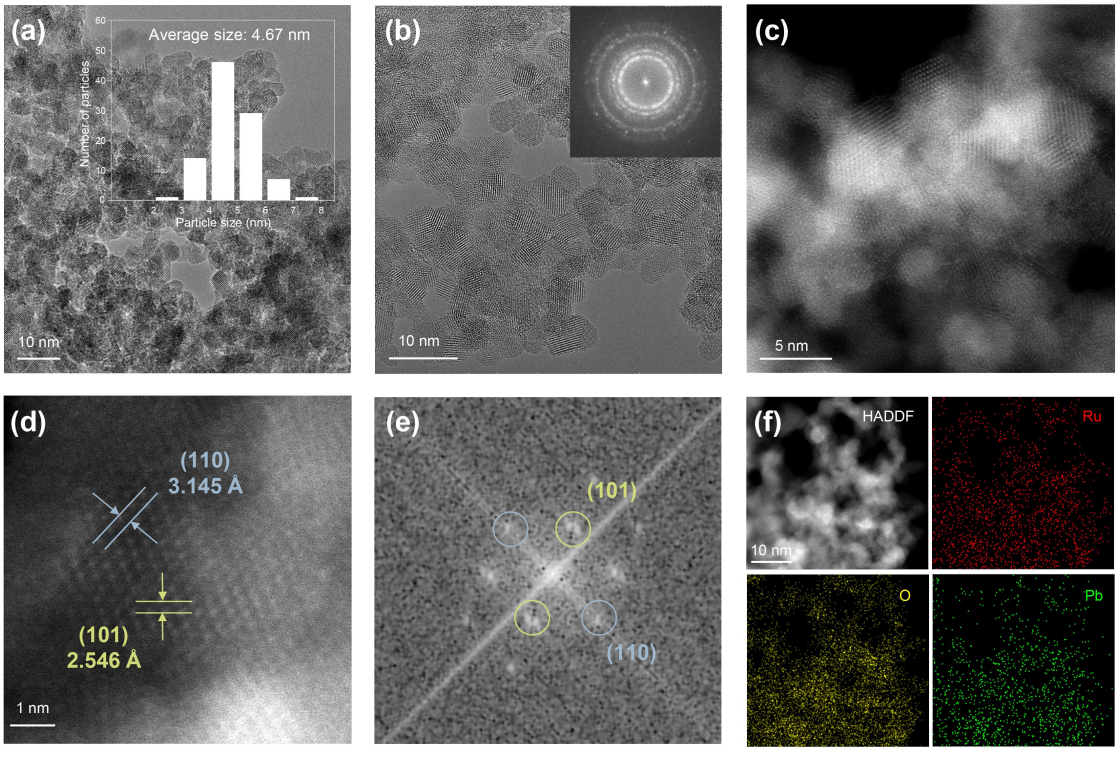

presumably impact crystallinity and phase segregation. A comparison of performance in RDE tests revealed that an annealing temperature of 350 °C yielded the most active Ru_3PbOx OER catalyst (Fig. S2 in the ESM).

After the aforementioned optimization, we performed a series of characterizations to examine the morphology and structure of the synthesized catalyst. First, high resolution transmission electron microscopy (TEM) was utilized to measure the size of nanoparticles. The TEM image (Fig. 1(a), Figs. S3 and S4 in the ESM) unveils that the size of Ru_3PbOx particles is uniform, with an average size of ~4.67 nm, and the fast Fourier transform (FFT) pattern (Fig. 1(b)) indicates a polycrystalline structure of our catalyst. To further confirm the lattice distance, a high-angle annular dark-field scanning TEM (HAADF-STEM) was employed, confirming that the lattice distances and the corresponding FFT patterns are primarily correspond to the (110) and (101) facets of RuO_2 (Fig. 1(c-e) and Fig. S5 in the ESM). In addition, energy-dispersive spectroscopic (EDS) elemental mapping (Fig. 1(f) and Fig. S6 in the ESM) confirmed that the majority of Pb was uniformly doped within the RuO_2 matrix. Overall, these images reveal a nanoparticle structure with high crystallinity and uniform doping.

Figure 1 Morphology and structure characterizations of Ru_3PbOx. (a,b) TEM images of Ru_3PbOx nanoparticles. The average particle size is 4.67 nm as shown in the inset of (a), and the inset of (b) is a FFT pattern showing a polycrystalline property. (c,d) HADDF-STEM images of Ru_3PbOx. (c) is a low-magnification HADDF-STEM image, and (d) is a high-resolution image showing the high crystallinity with the lattice distant of 3.145 and 2.546 Å corresponding to the RuO_2 (110) and RuO_2 (101) facets, respectively. (e) the corresponding FFT pattern of (d). (f) EDS elemental mapping of Ru_3PbOx catalyst showing a uniform distribution of Ru and Pb.

Next, the X-ray diffraction (XRD) pattern was analyzed to unveil the detailed crystal structure of Ru_3PbOx. As shown in Figure 2(a), while the predominant peaks with the highest intensity indeed (110) and (101) facets of RuO_2, we did observe several minor peaks that could be attributed to various Pb oxides or the Pb-doped Ru oxide structure. This is likely due to the slight aggregation of Pb oxides into tiny clusters during the annealing process, which is challenging to observe in TEM. Furthermore, this pattern also indicates that the oxidation annealing step did not fully oxidize our Pb into PbO_2 within our pristine Ru_3PbOx catalyst. Notably, these Pb oxide peaks are later transformed into PbO_2 peaks in our post-catalysis XRD characterization, as explained in detail in the later section. Additionally, we analyzed the XRD patterns of different Ru-Pb oxide catalysts synthesized, and noted that the intensities of RuO_2 peaks can vary based on the ratio, while the peak positions remain nearly consistent (Fig. S7 in the ESM).

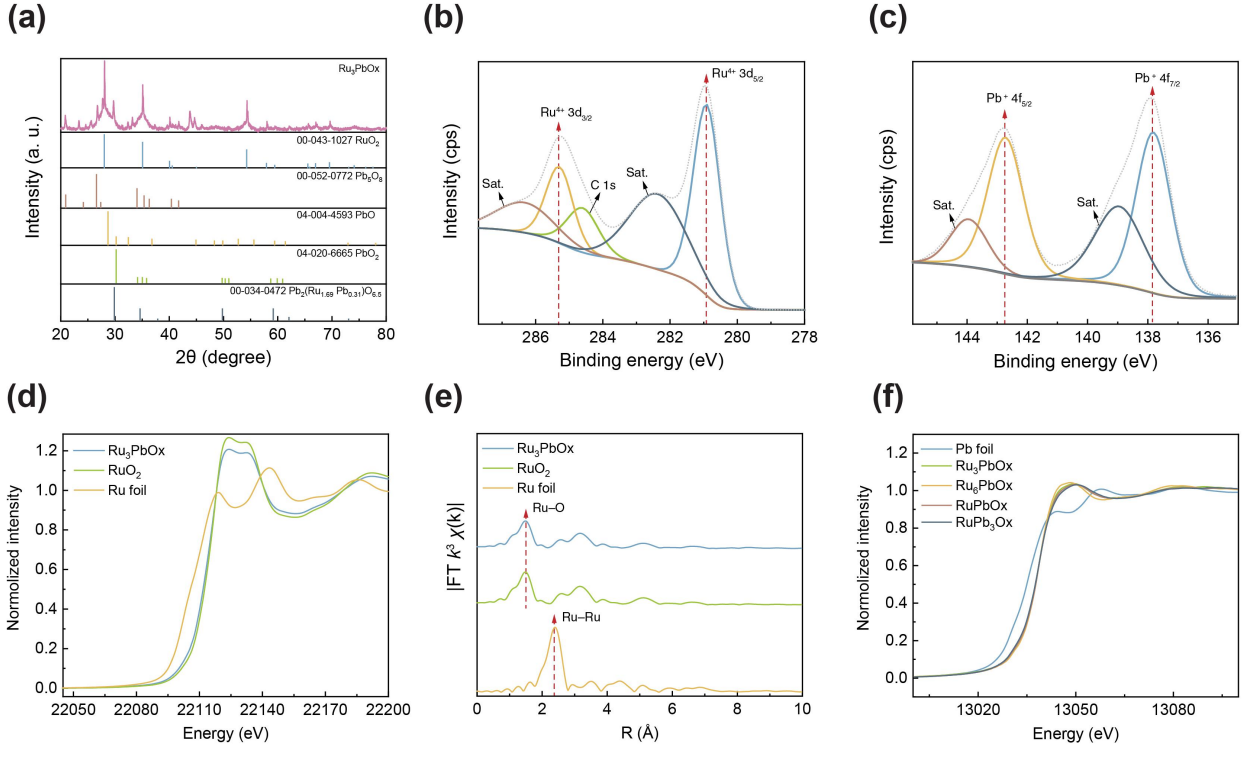

Figure 2 Electronic and crystal structure of Ru_3PbOx. (a) XRD patterns of Ru_3PbOx, showing a majority peaks corresponding to RuO_2 and the rest of the minor peaks to different structure of PbOx. (b,c) High-resolution XPS spectra of Ru *3d*

(b) and Pb *4f* (c). (d,e) XANES (d) and EXAFS (e) spectra at Ru K-edge of Ru_3PbOx, indicating an oxidation state close to RuO_2 and a bonding structure with Ru–O and without Ru–Ru bonds. (f) XANES spectra at Pb L3-edge showing different ratio of Ru-Pb oxide nanoparticles with similar oxidation states and are all distinct from Pb foil.

Electronic properties of catalysts. After understanding the morphology and crystal structure of Ru_3PbOx, the next step involves carefully investigating its electronic properties, as these properties are commonly considered critical factors that can affect OER activity [32, 33]. We first conducted an X-ray photoelectron spectroscopy (XPS) survey spectrum of Ru_3PbOx to confirm the metal ratio between Ru and Pb (Fig. S8 in the ESM). The resulting ratio of Ru to Pb is 73:27, which is quite similar to the expected 3:1 ratio (Table S1 in the ESM). This ratio also indicates a mass ratio of Ru to Pb of 57:43 on the surface analyzed by XPS. The elemental ratio based on the EDS mapping analysis also indicates the bulk atomic ratio of Ru:Pb is around 3:1 as expected (Table S2 in the ESM). Different ratios of Ru-Pb oxides were also analyzed (Figs. S9, S10, and Table S1 in the ESM), and all of the ratios are similar to our expectations except for $RuPb_3Ox$, which has a lower Pb ratio than expected, potentially due to some Pb aggregations. Next, a thorough high-resolution XPS analysis of Ru 3d and Pb 4f (Figs. 2(b) and 2(c)) was conducted to understand the electronic structures of Ru and Pb in Ru_3PbOx, respectively. Figure 2(b) suggests the electronic state of Ru as Ru^{4+} based on the peaks of Ru $3d_{5/2}$, Ru $3d_{3/2}$, and their satellite peaks between 280 and 290 eV [18, 22, 23], which also matches the observations in TEM and XRD that Ru is in its close to the oxidation state as RuO_2. Figure 2(c) shows an oxidation state of Pb between Pb^{2+} (PbO) and Pb^{4+} (PbO_2) based on the Pb $4f_{7/2}$ and Pb $4f_{5/2}$ peaks. Notably, PbO and PbO_2 peaks exhibit a small difference of ~0.3 eV [34, 35], and the Pb 4f peaks here can likely be a combination of peaks from different Pb oxides that range from Pb^{2+} to Pb^{4+}, matching our observations in XRD.

Synchrotron-based X-ray absorption spectroscopy (XAS) measurements offer additional insight into the electronic properties of our catalyst. The rising edge of the Ru K-edge X-ray absorption near-edge spectroscopy (XANES) and its white line (Fig. 2(d) and Fig. S11 in the ESM) indicate that the electronic state of Ru in Ru_3PbOx, while quite close to the RuO_2 reference, might be slightly lower than Ru^{4+}. This might be due to the slightly higher electronegativity of Ru compared to Pb atoms in the synthesized bimetallic oxide. Although this could also be explained by the potential presence of metallic Ru clusters that were not fully oxidized during the annealing process, this possibility is further excluded by the corresponding Ru K-edge Fourier-transformed extended X-ray absorption fine structure (FT-EXAFS) in Figure 2(e). The FT-EXAFS result clearly shows a primary Ru–O peak (1.50 Å) and no Ru–Ru peak (2.39 Å), as evident in the reference spectrum of metallic Ru foil. Additionally, we examined different ratios of Ru-Pb oxides, and no significant differences in Ru K-edge XANES and EXAFS were observed, suggesting that the doping level of Pb ranging from approximately 15% to 44% does not significantly affect the electronic structure of Ru atoms. The XANES and EXAFS of Pb L3-edge were also investigated (Fig. 2(f), Figs. S14 and S15 in the ESM). The results reveal that the oxidation state of Ru_3PbOx is distinct from that of the reference Pb foil, displaying a pattern of Pb–O bonds without the presence of Pb–Pb peaks (Fig. S15 in the ESM). Furthermore, Pb L3-edge XAS spectra for various ratios of Ru-Pb oxides indicate similar oxidation states (Figs. S14 and S15 in the ESM), aligning with the XPS findings.

Electrochemical analysis on RDE. With a comprehensive understanding of the morphology and electronic structure, we then analyzed the fundamental electrochemical OER performance of the Ru_3PbOx catalyst. We compared our catalyst with commercial RuO_2 nanoparticles (denoted as "RuO_2 comm" in the figures). To ensure consistent performance comparisons in terms of nanoparticle size, we synthesized Ru oxide nanoparticles (denoted as RuO_2; see Methods and Fig. S16 in the ESM for more detail) using a similar procedure to that of Ru_3PbOx. Upon comparing the linear sweep voltammetry (LSV) curves in RDE under acidic conditions in 0.1 M $HClO_4$, we observed that Ru_3PbOx outperformed both RuO_2 and commercial RuO_2 (Fig. 3(a) and Table S3 in the ESM). The overpotential of Ru_3PbOx at 10 mA cm^{-2} is 201 mV, which is lower than RuO_2 (215 mV) and commercial RuO_2 (298 mV). Additionally, comparison of Tafel slopes (Fig. 3(b)) also reveals that Ru_3PbOx exhibits superior OER kinetics compared to the other two, with a Tafel slope of only 40.49 mV dec^{-1}. Furthermore, electrochemical impedance spectroscopy (EIS) results at 1.5 V versus the reversible hydrogen electrode (RHE) confirm that Ru_3PbOx has lower charge transfer resistance than the control Ru oxide samples (Fig. S17 in the ESM). Importantly, all tests in this study employ the same mass loading across different catalysts. Therefore, this suggests that even with the Ru loading lowered by ~40% in Ru_3PbOx compared to the Ru oxide samples, the activity of Ru_3PbOx remains significantly superior to those with higher Ru loading.

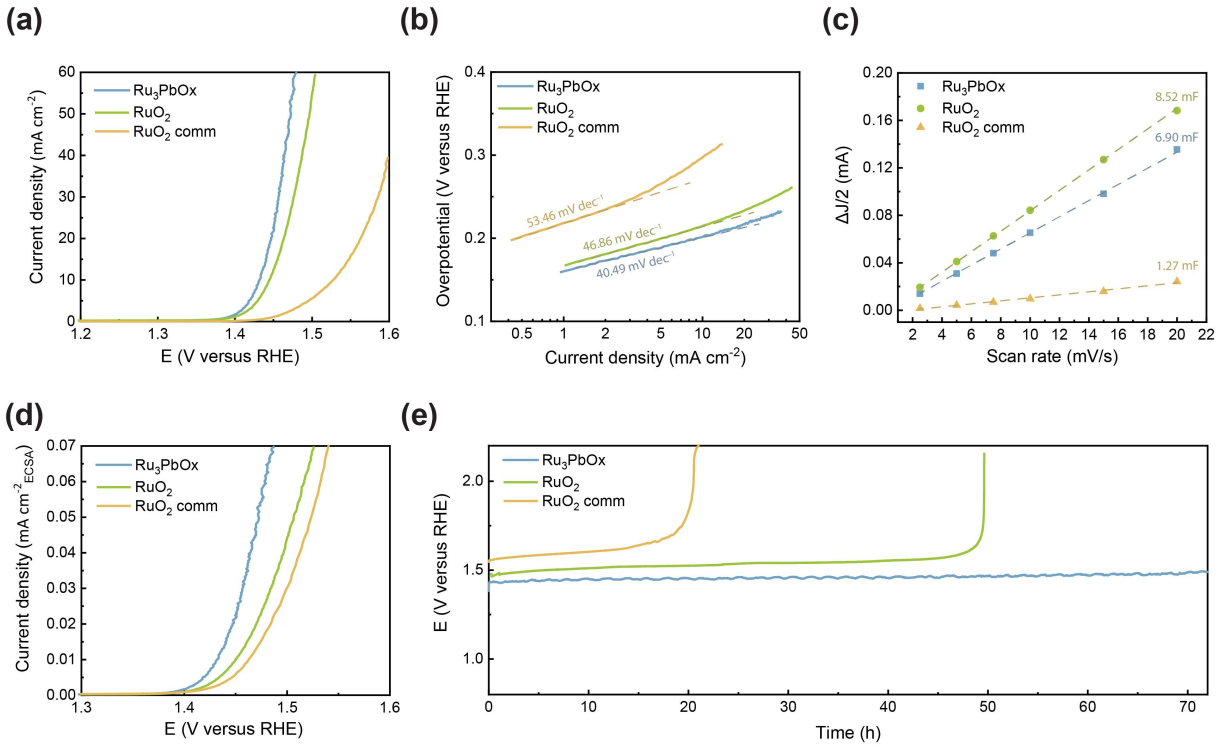

Figure 3 Acidic OER performance on RDE. (a,b) LSV curves (a) and Tafel slopes (b) of Ru_3PbOx, RuO_2, and commercial RuO_2. (c) C_{dl} plots for ECSA analysis derived from CV curves in Supplementary Figs. 18a-c. (d) ECSA-corrected LSVs of Ru_3PbOx, RuO_2, and commercial RuO_2, showing Ru_3PbOx has a better intrinsic activity. (e) Stability tests of Ru_3PbOx, RuO_2, and commercial RuO_2on RDE at 10 mA cm^{-2}.

It is known that an improvement in activity of electrocatalysts can be attributed to the higher surface area instead of the improvement in intrinsic activity that is due to the well-tuned active site. To confirm whether it is the case for Ru_3PbOx, we conducted ECSA analysis by measuring the electrochemical double-layer capacitance (C_{dl}) of our catalysts (Fig. S18 in the ESM). Although Ru_3PbOx shows a better activity above, the C_{dl} results suggest that ECSA of Ru_3PbOx is lower than the RuO_2 nanoparticle control sample (Fig. 3(c) and Table S4 in the ESM). This means that if we consider the ECSA-normalized OER activities (Fig. 3(d)), Ru_3PbOx clearly shows a better intrinsic activity compared to the pure RuO_2 samples. It is presumably due to the electronic structure tuning from the Pb dopant in the RuO_2 lattice that enhances the intrinsic performance of Ru active sites. Different ratios of Ru-Pb oxide samples were also compared (Figs. S19 and S20 in the ESM), and the results confirm that the 3:1 ratio of Ru to Pb offers the best intrinsic activity, followed by the ratios of 6:1, 1:1, and 1:3,

respectively.

On top of activity, stability is, in fact, a more critical merit for acidic OER catalysts in practical PEM-WE applications [13, 14]. Therefore, stability tests on RDE were performed to gain an initial understanding of the catalysts under a lab-scale environment. Long-term chronopotentiometry (CP) stability results (Fig. 3(e)) show that Ru_3PbOx can last for over 72 hours without significant degradation at a current density of 10 mA cm^{-2}. Meanwhile, under the same total mass loading as commercial RuO_2 and RuO_2 that we synthesized using the same method (equivalent to a Ru loading around 1.6 times higher than Ru_3PbOx), sharp degradation can be observed around 20 and 50 hours, respectively. This suggests that not only the improvement in activity but also the Pb dopant as a supporting element is likely to help maintain the stability of RuO_2 active sites.

Stability performance in PEM-WE. In addition to the initial stability analysis in lab-scale RDE test, it is more important to investigate the stability in a practical PEM-WE device to evaluate Ru_3PbOx as an anodic OER catalyst. Our self-fabricated compact PEM-WE device (Figs. 4(a) and 4(b)) operates by introducing deionized water through the anode inlet for OER, utilizing Ru_3PbOx as the catalyst. Protons are transported across the membrane for the cathodic hydrogen evolution reaction (HER), facilitated by Pt/C as the catalyst. Over the Ru_3PbOx catalyst-coated membrane (CCM) with a predetermined total mass loading of ~2 mg cm^{-2}, a porous transport layer composed of Ti frit and Carbon paper is employed for the anode and cathode, respectively (refer to Methods for a detailed description). A CP test at 100 mA cm^{-2} was conducted under ambient pressure and room temperature (Fig. 4(c)), revealing that the Ru_3PbOx catalyst could sustain stable performance for over 300 h without any notable voltage decay. We have observed that the voltage here is slightly higher than expected when compared to the strong intrinsic activity observed in the RDE test. This divergence could be attributed to either a less mature PEM-WE assembly technique leading to increased ohmic resistance or the harsher acidic environment on the PEM compared to the RDE setup, potentially causing reduced performance.

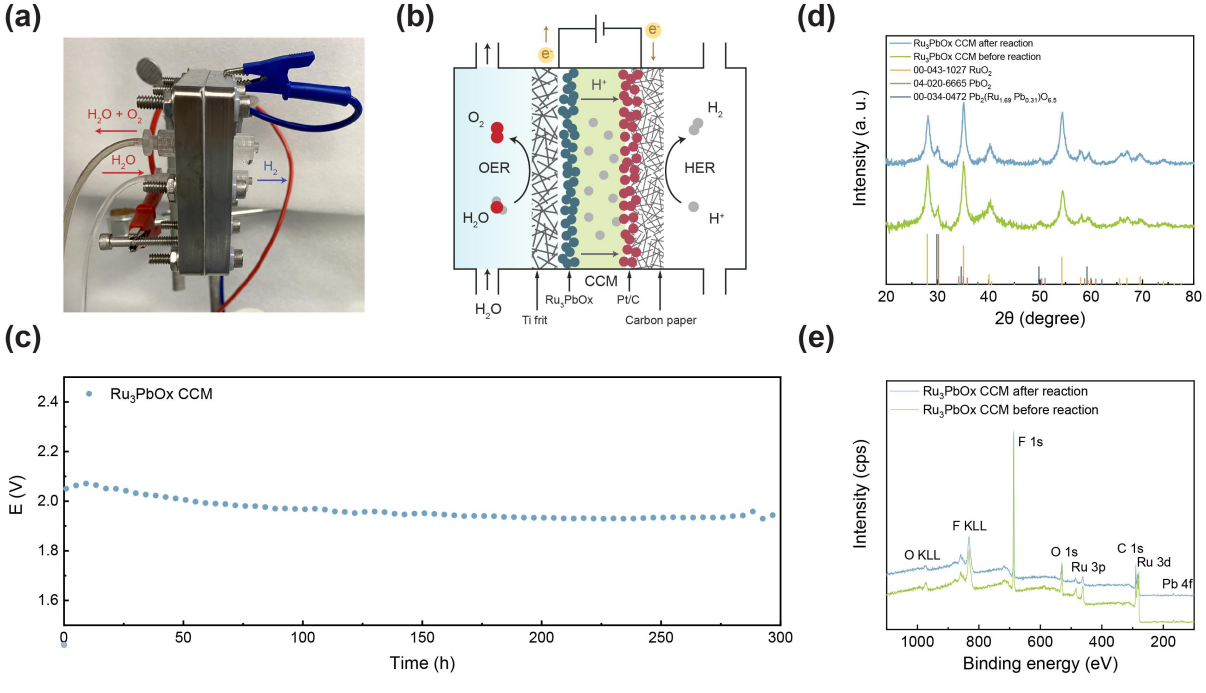

Figure 4 Stability of Ru_3PbOx in PEM-WE. (a,b) Photograph (a) and schematic (b) of the PEM-WE setup of our stability test. (c) Chronopotentiometry tests of Ru_3PbOx catalysts on CCM at 100 mA cm^{-2} in the PEM-WE electrolyzer using commercial Pt/C as the cathode catalyst at room temperature and ambient pressure. (d,e) XRD patterns (d) and XPS survey spectra (e) of Ru_3PbOx CCM before reaction and after the 300 h stability test in PEM-WE, showing no significant voltage increases.

Finally, we conducted post-catalysis characterizations to verify the actual active structure following the 300 h stability test in the PEM-WE system. Both the Ru_3PbOx CCM before and after the reaction were collected and investigated. XRD patterns reveal that after the Ru_3PbOx coating on the membrane and subsequent activation via boiling (as described in Methods), the major peaks are attributed to RuO_2, while minor peaks indicate the presence of PbO_2 and a bimetallic Pb-Ru oxide (Fig. 4(d)). Notably, there is no significant change observed before and after the extended stability test, suggesting the maintenance of a stable crystal

structure in the catalyst. XPS survey spectra also support this conclusion (Fig. 4(e)), and high-resolution Ru 3d and Pb 4f XPS spectra further confirm that the peaks do not shift before and after the reaction (S21). Collectively, these findings provide evidence of the stable performance of Ru_3PbOx in a practical PEM-WE device.

In summary, we developed a Ru-based catalyst with Pb dopant as a supporting element for acidic OER. This catalyst reduces the Ru loading by ~40%, while simultaneously delivering improved performance in both stability and intrinsic activity compared to the RuO_2 catalyst. Electrochemical analysis in RDE demonstrated that the Ru_3PbOx catalyst exhibits an OER overpotential as low as 201 mV at 10 mA cm^{-2}, and a practical stability test in PEM-WE showed a long-term stability of over 300 h at 100 mA cm^{-2}. Future research can advance catalyst development to further decrease noble metal loading while striving for enhanced stability, which will be crucial in lowering the green hydrogen price for the future energy landscape.

Method

Catalyst synthesis. In general, to synthesize the main Ru_3PbOx catalyst, 0.1231 g of $RuCl_3$ and 0.0639 g of $Pb(NO_3)_2$ (i.e. Ru and Pb with a molar ratio of 3:1) were dissolved in 150 mL of 1 M HCl with sonication for 3 h. Then, 0.4 g of carbon black (Cabot, BP2000) was added, and the mixture was stirred for 18 h under ambient conditions. The well-mixed solution was then dried by a rotary evaporator. The remaining powder was collected and annealed in a flowing Ar/H_2 (5% H_2) atmosphere at 1000 °C for 2 h and then in air at 250-550 °C for 3 h, where the temperature at 350 °C in air was identified to synthesize the most active Ru_3PbOx catalyst. The annealed sample was collected and denoted as the Ru_3PbOx catalyst. Different ratios of Ru-Pb oxide ($Ru_xPb_yO_z$) were synthesized following the same method, except the initial amount of precursors were added based on the desired molar ratio of Ru:Pb. The RuO_2 control sample was prepared using the same method with $RuCl_3$ as the precursor, and maintaining the total metal mass loading equivalent to the sum of Ru and Pb in the Ru-Pb catalysts. The weight ratio of total metal loading in precursors to carbon black was fixed at 1:4 for all the catalysts above.

Material characterization. TEM, HRTEM, HADDF-STEM, and EDS mapping were performed using an FEI Titan Themis aberration-corrected TEM at 300 kV. XPS data were measured on a PHI Quantera spectrometer using monochromatic Al Kα radiation (1,486.6 eV) and a low-energy flood gun as the neutralizer. The XPS spectra were calibrated based on the detected carbon C 1*s* peak at a standard of 284.8 eV. XRD data were collected on a Rigaku SmartLab X-ray diffractometer with Cu Kα radiation. XAS measurements were conducted at the Sector 20-BM beamline of the Advanced Photon Source at Argonne National Laboratory. The samples were measured in transmission mode simultaneously with Ru and Pb foils as references, and the data processing for FT-EXAFS was performed using the ATHENA program.

Electrochemical measurements under a three-electrode system. In a typical test, 5 mg of catalyst was added into 1 mL isopropyl alcohol and 20 μL of Nafion 117 containing solution (5%, Sigma-Aldrich), and the mixture was then sonicated for 1 h to obtain a well-dispersed catalyst ink. For a typical RDE measurement, 16 μL of the catalyst ink was drop-casted on a 5.0 mm diameter glassy carbon electrode (disk geometric area: 0.196 cm^2), resulting in a catalyst loading of 0.4 mg cm^{-2}, and then vacuum dried at room temperature before the test. All the RDE measurements were performed at room temperature in a typical three-electrode cell in O_2-saturated 0.1 M $HClO_4$ electrolyte. A carbon rod (99.99 %, Beantown Chemical) and a saturated calomel electrode (SCE, CH Instruments) were used as the counter and reference electrode, respectively. A RDE assembly (AFE4TQ050, Pine Instruments) with the prepared glassy carbon electrode was used as the working electrode at a rotation rate of 2500 revolutions per minute. All potentials measured against SCE were converted to the reversible hydrogen electrode (RHE) scale by: E (versus RHE) = E (versus SCE) + 0.241 V + 0.0591×pH. In the 0.1 M $HClO_4$ electrolyte in this work, the pH value was 1, as measured by Orion Star A111 pH Meter (Thermo Scientific). Solution resistance (Rs) was measured by potentiostatic electrochemical impedance spectroscopy (PEIS) at frequencies from 0.1 Hz to 200 kHz. All the measured potentials in RDE were 100% *iR*-compensated unless otherwise specified. LSV tests were recorded at a scan rate of 5 mV s^{-1}. Stability was examined through chronopotentiometry tests at 10 mA cm^{-2}. Electrochemical impedance spectroscopy (EIS) tests for Nyquist plot were performed at 1.5 V (versus RHE) from 0.1 Hz to 200 kHz. The ECSA was determined by: $ECSA = C_{dl}/C_s$, where C_{dl} is the double layer capacitance and C_s is the specific capacitance of the sample. In this study, a general specific capacitance of C_s = 0.035 mF cm^{-2} was used based on typical reported values [22]. C_{dl} was determined by the equation: $C_{dl} = i_c/\nu$, where i_c is the charging current and ν is the scan rate. A series of CV

tests in the non-faradaic potential region 1.18-1.28 V (versus RHE) under different scan rates (2.5 mV s^{-1}, 5.0 mV s^{-1}, 7.5 mV s^{-1}, 10 mV s^{-1}, 15 mV $s^{-1}$and 20 mV s^{-1}) were performed, and by plotting the measured i_c versus ν. The Cdl was obtained from the slopes of the linear fitting in Figs. S18 and S19 in the ESM. The roughness factor (RF) was calculated by dividing ECSA by the geometric area of the electrode, which is 0.196 cm^{-2} in this study.

PEM-WE tests. A single-side catalyst coated membrane (CCM) with anode catalyst layer was used in PEM electrolyzer. To make the ink for spray coating, the anode catalyst Ru_3PbOx was dispersed in isopropyl alcohol, then Nafion ionomer solution (5%, Sigma-Aldrich) was added to the mixture. To make the cathode ink for spray coating, Pt/C (Pt content 20%) was mixed with water first to avoid combustion, then IPA and Nafion ionomer solution was added to the mixture. The weight ratio of ionomer to catalyst was 0.2 for both anode and cathode. The anode ink was sonicated for 2 hours before sprayed onto a piece of Nafion 115 membrane by air brush, and the cathode ink was sprayed onto a carbon paper electrode. The anode and cathode catalyst loadings were controlled at 2 mg cm^{-2} and 0.8 mg cm^{-2}, respectively. The CCM was then boiled in water for 1.5 hours to fully remove impurities. To assemble the membrane electrode assembly (MEA), the CCM was sandwiched between a platinized Ti fiber felt and the cathode electrode, with anode catalyst layer facing the Ti felt side. The active area was 1 cm^{-2}. The anode and cathode electrodes were fixed by polytetrafluoroethylene gaskets of 0.01 inch and 0.005 inch, respectively. Finally, the gaskets, electrodes and CCM were sandwiched between an anode end plate made of Ti and a cathode end plate made of stainless steel, both of which with serpentine flow channel. Room temperature deionized water was first fed to the anode at a flow rate of 0.4 mL min^{-1} for 30 min before the test, and continuously flowed during the test. The stability test was carried out at 100 mA cm^{-2} at room temperature and ambient pressure.

Acknowledgements

This work was supported by the Robert A. Welch Foundation (grant no. C-2051-20230405), the David and Lucile Packard Foundation (grant no. 2020-71371), and the Alfred P. Sloan Foundation (grant no. FG-2021-15638).

Electronic Supplementary Material: Supplementary information (Figs. S1 to S21 and Tables S1 to S4) is available in the online version of this article at http://dx.doi.org/10.1007/s12274-***-****-*

References

[1] Seh, Z. W.; Kibsgaard, J.; Dickens, C. F.; Chorkendorff, I.; Nørskov, J. K.; Jaramillo, T. F. Combining theory and experiment in electrocatalysis: Insights into materials design. *Science* **2017**, *355*, eaad4998.

[2] Jiao, Y.; Zheng, Y.; Jaroniec, M.; Qiao, S. Z. Design of electrocatalysts for oxygen- and hydrogen-involving energy conversion reactions. *Chem. Soc. Rev.* **2015**, *44*, 2060–2086.

[3] De Luna, P.; Hahn, C.; Higgins, D.; Jaffer, S. A.; Jaramillo, T. F.; Sargent, E. H. What would it take for renewably powered electrosynthesis to displace petrochemical processes? *Science* **2019**, *364*, eaav3506.

[4] Chow, J.; Kopp, R. J.; Portney, P. R. Energy Resources and Global Development. *Science* **2003**, *302*, 1528–1531.

[5] Chen, L.; Dong, X.; Wang, Y.; Xia, Y. Separating hydrogen and oxygen evolution in alkaline water electrolysis using nickel hydroxide. *Nat. Commun.* **2016**, *7*, 11741.

[6] Lei, Z.; Wang, T.; Zhao, B.; Cai, W.; Liu, Y.; Jiao, S.; Li, Q.; Cao, R.; Liu, M. Recent Progress in Electrocatalysts for Acidic Water Oxidation. *Adv. Energy Mater.* **2020**, *10*, 2000478.

[7] Carmo, M.; Fritz, D. L.; Mergel, J.; Stolten, D. A comprehensive review on PEM water electrolysis. *Int. J. Hydrogen Energy* **2013**, *38*, 4901–4934.

[8] An, L.; Wei, C.; Lu, M.; Liu, H.; Chen, Y.; Scherer, G. G.; Fisher, A. C.; Xi, P.; Xu, Z. J.; Yan, C.-H. Recent Development of Oxygen Evolution Electrocatalysts in Acidic Environment. *Adv. Mater.* **2021**, *33*, 2006328.

[9] Peng, Y.; Jiang, K.; Hill, W.; Lu, Z.; Yao, H.; Wang, H. Large-Scale, Low-Cost, and High-Efficiency Water-Splitting System for Clean H_2 Generation. *ACS Appl. Mater. Interfaces* **2019**, *11*, 3971–3977.

[10] Lettenmeier, P.; Wang, R.; Abouatallah, R.; Helmly, S.; Morawietz, T.; Hiesgen, R.; Kolb, S.; Burggraf, F.; Kallo, J.; Gago, A. S.; Friedrich, K. A. Durable Membrane Electrode Assemblies for Proton Exchange Membrane Electrolyzer Systems Operating at High Current Densities. *Electrochim. Acta* **2016**, *210*, 502–511.

[11] King, L. A.; Hubert, M. A.; Capuano, C.; Manco, J.; Danilovic, N.; Valle, E.; Hellstern, T. R.; Ayers, K.; Jaramillo, T. F. A non-precious metal hydrogen catalyst in a commercial polymer electrolyte membrane electrolyser. *Nat. Nanotechnol.* **2019**, *14*, 1071–1074.

[12] Spöri, C.; Kwan, J. T. H.; Bonakdarpour, A.; Wilkinson, D. P.; Strasser, P. The Stability Challenges of Oxygen Evolving Catalysts: Towards a Common Fundamental Understanding and Mitigation of Catalyst Degradation. *Angew. Chem. Int. Ed.* **2017**, *56*, 5994–6021.

[13] Geiger, S.; Kasian, O.; Ledendecker, M.; Pizzutilo, E.; Mingers, A. M.; Fu, W. T.; Diaz-Morales, O.; Li, Z.; Oellers, T.; Fruchter, L.; Ludwig, A.; Mayrhofer, K. J. J.; Koper, M. T. M.; Cherevko, S. The stability number as a metric for electrocatalyst stability benchmarking. *Nat. Catal.* **2018**, *1*, 508–515.

[14] Chen, F.-Y.; Wu, Z.-Y.; Adler, Z.; Wang, H. Stability challenges of electrocatalytic oxygen evolution reaction: From mechanistic understanding to reactor design. *Joule* **2021**, *5*, 1704–1731.

[15] Milosevic, M.; Böhm, T.; Körner, A.; Bierling, M.; Winkelmann, L.; Ehelebe, K.; Hutzler, A.; Suermann, M.; Thiele, S.; Cherevko, S. In Search of Lost Iridium: Quantification of Anode Catalyst Layer Dissolution in Proton Exchange Membrane Water Electrolyzers. *ACS Energy Lett.* **2023**, *8*, 2682–2688.

[16] Diaz-Morales, O.; Raaijman, S.; Kortlever, R.; Kooyman, P. J.; Wezendonk, T.; Gascon, J.; Fu, W. T.; Koper, M. T. M. Iridium-based double perovskites for efficient water oxidation in acid media. *Nat. Commun.* **2016**, *7*, 12363.

[17] Zheng, Y.-R.; Vernieres, J.; Wang, Z.; Zhang, K.; Hochfilzer, D.; Krempl, K.; Liao, T.-W.; Presel, F.; Altantzis, T.; Fatermans, J.; Scott, S. B.; Secher, N. M.; Moon, C.; Liu, P.; Bals, S.; Van Aert, S.; Cao, A.; Anand, M.; Nørskov, J. K.; Kibsgaard, J.; Chorkendorff, I. Monitoring oxygen production on mass-selected iridium–tantalum oxide electrocatalysts. *Nat.*

Energy **2021**, *7*, 55–64

[18] Yao, Y.; Hu, S.; Chen, W.; Huang, Z.-Q.; Wei, W.; Yao, T.; Liu, R.; Zang, K.; Wang, X.; Wu, G.; Yuan, W.; Yuan, T.; Zhu, B.; Liu, W.; Li, Z.; He, D.; Xue, Z.; Wang, Y.; Zheng, X.; Dong, J.; Chang, C.-R.; Chen, Y.; Hong, X.; Luo, J.; Wei, S.; Li, W.-X.; Strasser, P.; Wu, Y.; Li, Y. Engineering the electronic structure of single atom Ru sites via compressive strain boosts acidic water oxidation electrocatalysis. *Nat. Catal.* **2019**, *2*, 304–313.

[19] Wen, Y.; Chen, P.; Wang, L.; Li, S.; Wang, Z.; Abed, J.; Mao, X.; Min, Y.; Dinh, C. T.; Luna, P. D.; Huang, R.; Zhang, L.; Wang, L.; Wang, L.; Nielsen, R. J.; Li, H.; Zhuang, T.; Ke, C.; Voznyy, O.; Hu, Y.; Li, Y.; Goddard Iii, W. A.; Zhang, B.; Peng, H.; Sargent, E. H. Stabilizing Highly Active Ru Sites by Suppressing Lattice Oxygen Participation in Acidic Water Oxidation. *J. Am. Chem. Soc.* **2021**, *143*, 6482–6490.

[20] Jin, H.; Choi, S.; Bang, G. J.; Kwon, T.; Kim, H. S.; Lee, S. J.; Hong, Y.; Lee, D. W.; Park, H. S.; Baik, H.; Jung, Y.; Yoo, S. J.; Lee, K. Safeguarding the RuO_2 phase against lattice oxygen oxidation during acidic water electrooxidation. *Energy Environ. Sci.* **2022**, *15*, 1119–1130

[21] Retuerto, M.; Pascual, L.; Calle-Vallejo, F.; Ferrer, P.; Gianolio, D.; Pereira, A. G.; García, Á.; Torrero, J.; Fernández-Díaz, M. T.; Bencok, P.; Peña, M. A.; Fierro, J. L. G.; Rojas, S. Na-doped ruthenium perovskite electrocatalysts with improved oxygen evolution activity and durability in acidic media. *Nat. Commun.* **2019**, *10*, 2041.

[22] Lin, Y.; Tian, Z.; Zhang, L.; Ma, J.; Jiang, Z.; Deibert, B. J.; Ge, R.; Chen, L. Chromium-ruthenium oxide solid solution electrocatalyst for highly efficient oxygen evolution reaction in acidic media. *Nat. Commun.* **2019**, *10*, 162.

[23] Hao, S.; Liu, M.; Pan, J.; Liu, X.; Tan, X.; Xu, N.; He, Y.; Lei, L.; Zhang, X. Dopants fixation of Ruthenium for boosting acidic oxygen evolution stability and activity. *Nat. Commun.* **2020**, *11*, 5368.

[24] Wu, Z.-Y.; Chen, F.-Y.; Li, B.; Yu, S.-W.; Finfrock, Y. Z.; Meira, D. M.; Yan, Q.-Q.; Zhu, P.; Chen, M.-X.; Song, T.-W.; Yin, Z.; Liang, H.-W.; Zhang, S.; Wang, G.; Wang, H. Non-iridium-based electrocatalyst for durable acidic oxygen evolution reaction in proton exchange membrane water electrolysis. *Nat. Mater.* **2023**, *22*, 100–108.

[25] Shi, Z.; Li, J.; Wang, Y.; Liu, S.; Zhu, J.; Yang, J.; Wang, X.; Ni, J.; Jiang, Z.; Zhang, L.; Wang, Y.; Liu, C.; Xing, W.; Ge, J. Customized reaction route for ruthenium oxide towards stabilized water oxidation in high-performance PEM electrolyzers. *Nat. Commun.* **2023**, *14*, 843.

[26] Jin, H.; Liu, X.; An, P.; Tang, C.; Yu, H.; Zhang, Q.; Peng, H.-J.; Gu, L.; Zheng, Y.; Song, T.; Davey, K.; Paik, U.; Dong, J.; Qiao, S.-Z. Dynamic rhenium dopant boosts ruthenium oxide for durable oxygen evolution. *Nat. Commun.* **2023**, *14*, 354.

[27] Lin, C.; Li, J.-L.; Li, X.; Yang, S.; Luo, W.; Zhang, Y.; Kim, S.-H.; Kim, D.-H.; Shinde, S. S.; Li, Y.-F.; Liu, Z.-P.; Jiang, Z.; Lee, J.-H. In-situ reconstructed Ru atom array on α-MnO2 with enhanced performance for acidic water oxidation. *Nat. Catal.* **2021**, *4*, 1012–1023.

[28] Liu, H.; Zhang, Z.; Fang, J.; Li, M.; Sendeku, M. G.; Wang, X.; Wu, H.; Li, Y.; Ge, J.; Zhuang, Z.; Zhou, D.; Kuang, Y.; Sun, X. Eliminating over-oxidation of ruthenium oxides by niobium for highly stable electrocatalytic oxygen evolution in acidic media. *Joule* **2023**, *7*, 558–573.

[29] Cui, X.; Ren, P.; Ma, C.; Zhao, J.; Chen, R.; Chen, S.; Rajan, N. P.; Li, H.; Yu, L.; Tian, Z.; Deng, D. Robust Interface Ru Centers for High-Performance Acidic Oxygen Evolution. *Adv. Mater.* **2020**, *32*, 1908126.

[30] Li, N.; Keane, T. P.; Veroneau, S. S.; Hadt, R. G.; Hayes, D.; Chen, L. X.; Nocera, D. G. Template-stabilized oxidic nickel oxygen evolution catalysts. *Proceedings of the National Academy of Sciences* **2020**, *117*, 16187–16192.

[31] Huynh, M.; Ozel, T.; Liu, C.; Lau, E. C.; Nocera, D. G. Design of template-stabilized active and earth-abundant oxygen evolution catalysts in acid. *Chem. Sci.* **2017**, *8*, 4779–4794.

[32] Wu, T.; Sun, S.; Song, J.; Xi, S.; Du, Y.; Chen, B.; Sasangka, W. A.; Liao, H.; Gan, C. L.; Scherer, G. G.; Zeng, L.; Wang, H.; Li, H.; Grimaud, A.; Xu, Z. J. Iron-facilitated dynamic active-site generation on spinel $CoAl_2O_4$ with self-termination of surface reconstruction for water oxidation. *Nat. Catal.* **2019**, *2*, 763–772.

[33] Liu, J.; Hu, Q.; Wang, Y.; Yang, Z.; Fan, X.; Liu, L.-M.; Guo, L. Achieving delafossite analog by in situ electrochemical self-reconstruction as an oxygen-evolving catalyst. *Proceedings of the National Academy of Sciences* **2020**, *117*, 21906–21913.

[34] Pederson, L. R. Two-dimensional chemical-state plot for lead using XPS. *J. Electron. Spectrosc. Relat. Phenom.* **1982**, *28*, 203–209.

[35] Morgan, W. E.; Van Wazer, J. R. Binding energy shifts in the x-ray photoelectron spectra of a series of related Group IVa compounds. *J. Phys. Chem.* **1973**, *77*, 964–969.

Address correspondence to Haotian Wang, htwang@rice.edu

Electronic Supplementary Material

Ruthenium-Lead Oxide for Acidic Oxygen Evolution Reaction in Proton Exchange Membrane Water Electrolysis

Feng-Yang Chen[1†], Chang Qiu[1†], Zhen-Yu Wu[1†], Tae-Ung Wi[1], Y. Zou Finfrock[2], and Haotian Wang[1,3,4](✉)

[1] Department of Chemical and Biomolecular Engineering, Rice University, Houston, TX 77005, USA

[2] Structural Biology Center, X-ray Science Division, Argonne National Laboratory, Lemont, IL 60439, USA

[3] Department of Materials Science and NanoEngineering, Rice University, Houston, TX 77005, USA

[4] Department of Chemistry, Rice University, Houston, TX 77005, USA

[†] These authors contributed equally to this work

Supporting information to DOI 10.1007/s12274-****-****-* (automatically inserted by the publisher)

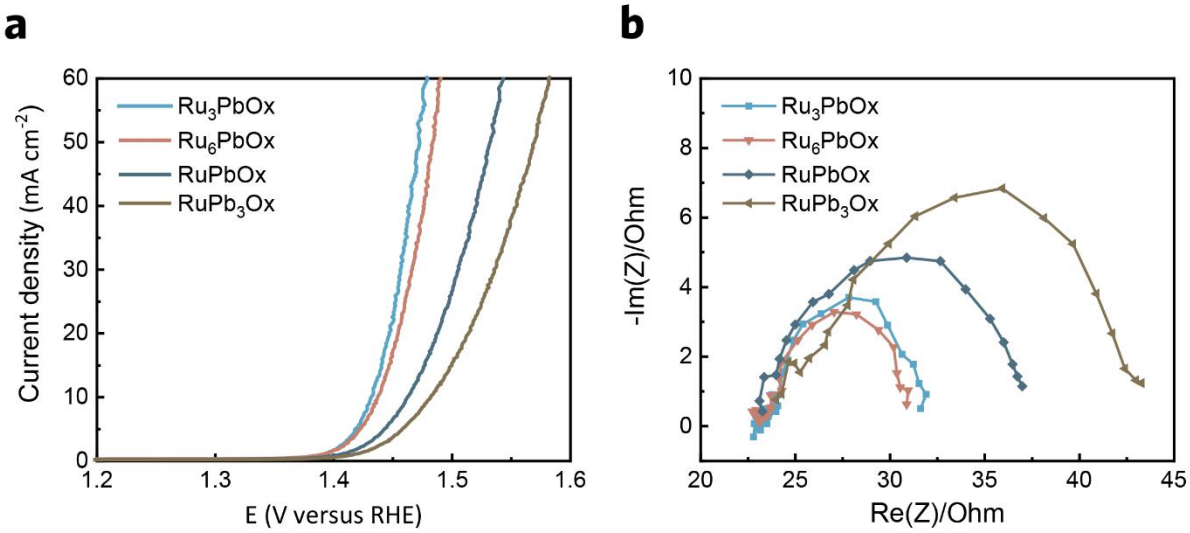

Figure S1. LSV curves (a) and EIS plots (b) of Ru_3PbOx, Ru_6PbOx, RuPbOx, $RuPb_3Ox$. Ru_3PbOx shows the best OER activity among these catalysts. In EIS plots (b), X-axis Re(Z) indicates the real part and Y-axis −Im(Z) indicates the imaginary part.

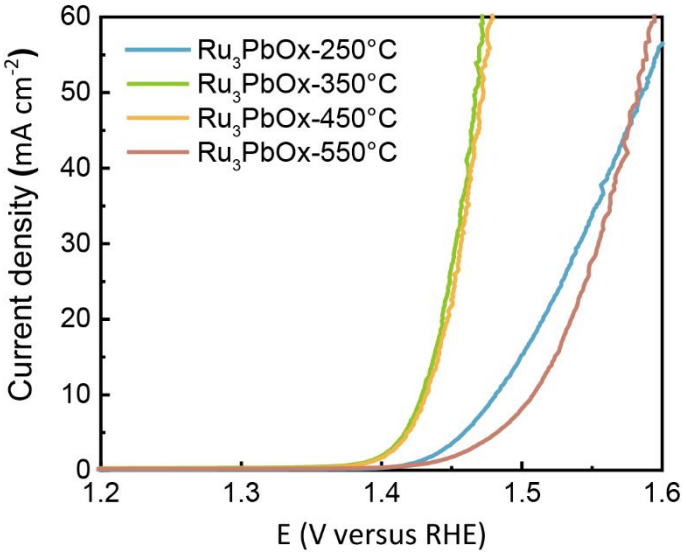

Figure S2. LSV curves of Ru_3PbOx catalysts annealed at different temperatures in air at the oxidation annealing step.

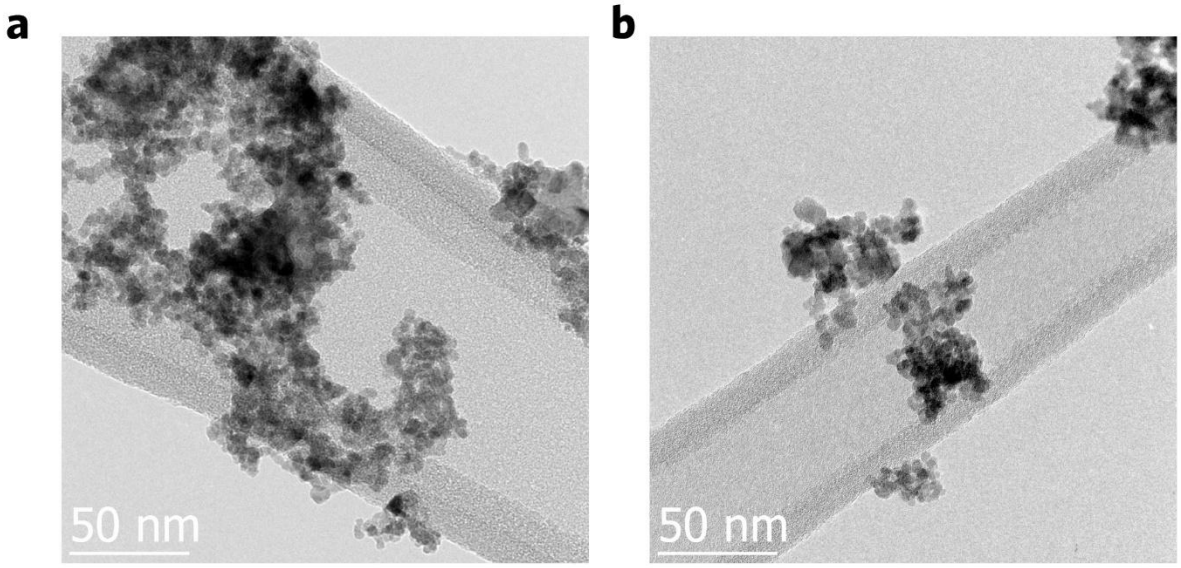

Figure S3. (a, b) TEM images of Ru_3PbOx nanoparticles using a JEOL 2100 Field Emission Gun TEM.

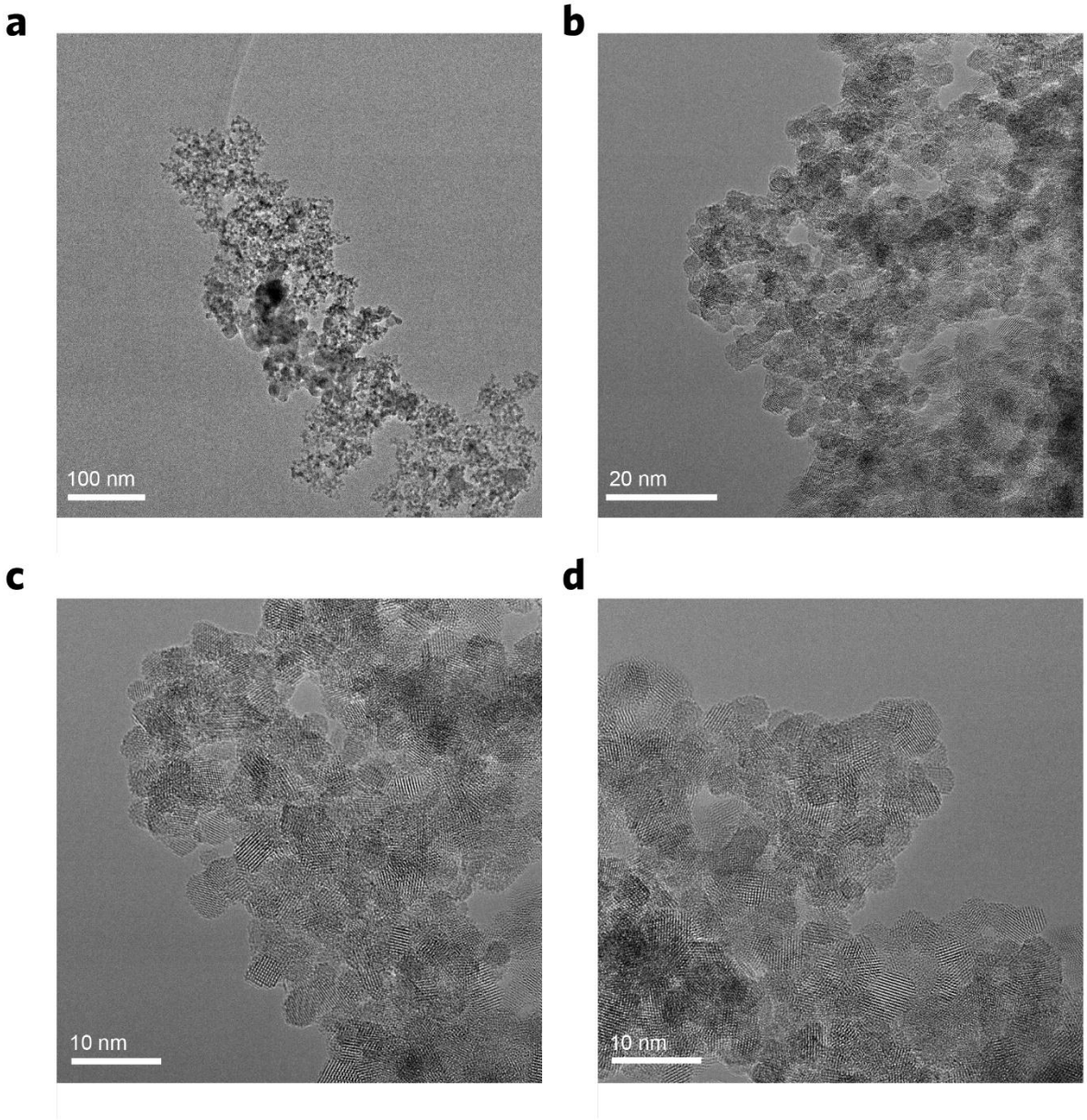

Figure S4. (a-d) TEM and high-resolution TEM (HRTEM) images of Ru_3PbOx nanoparticles using an FEI Titan Themis aberration-corrected TEM.

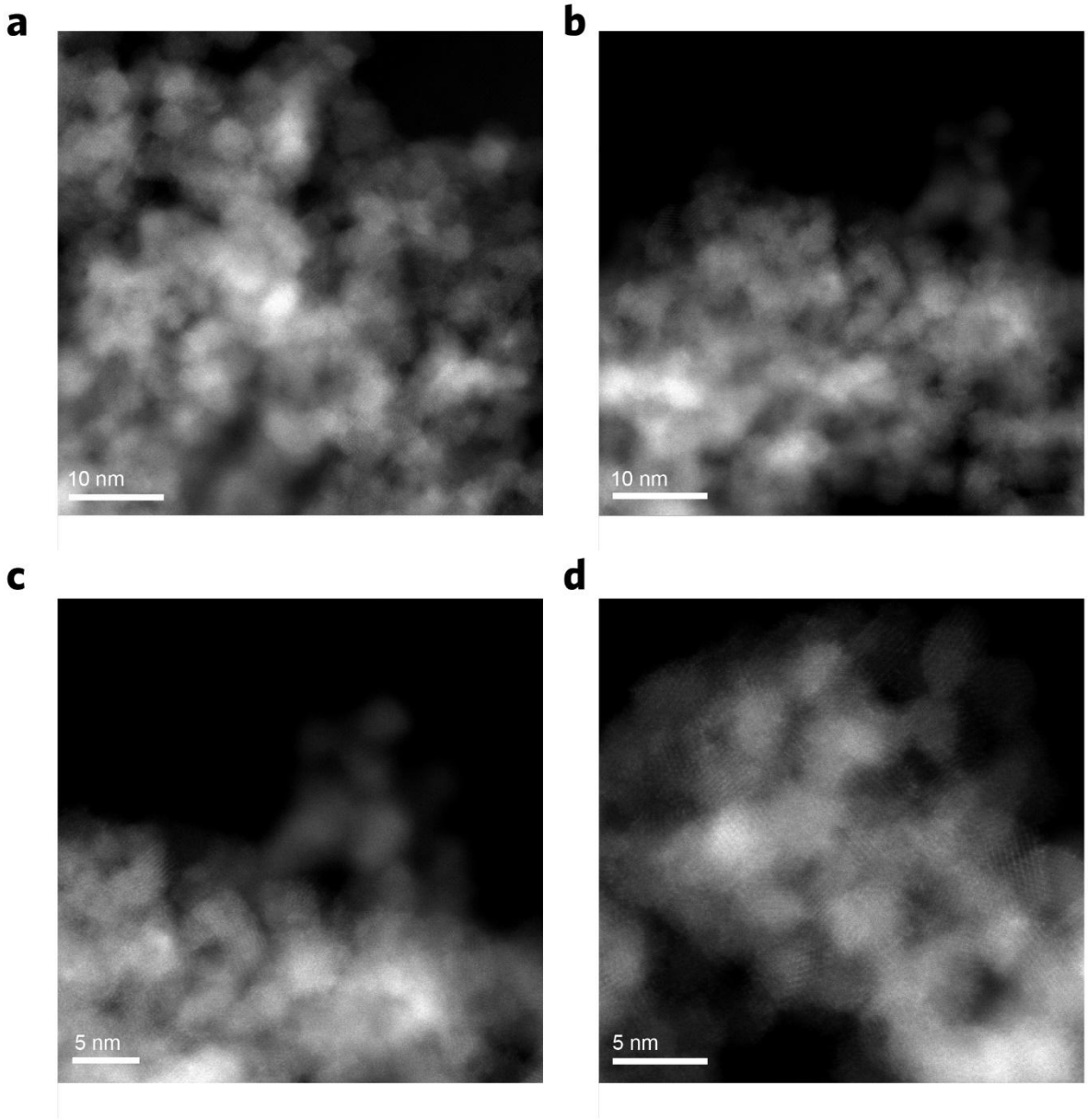

Figure S5. (a-d) HADDF-STEM images of Ru_3PbOx nanoparticles under different magnifications

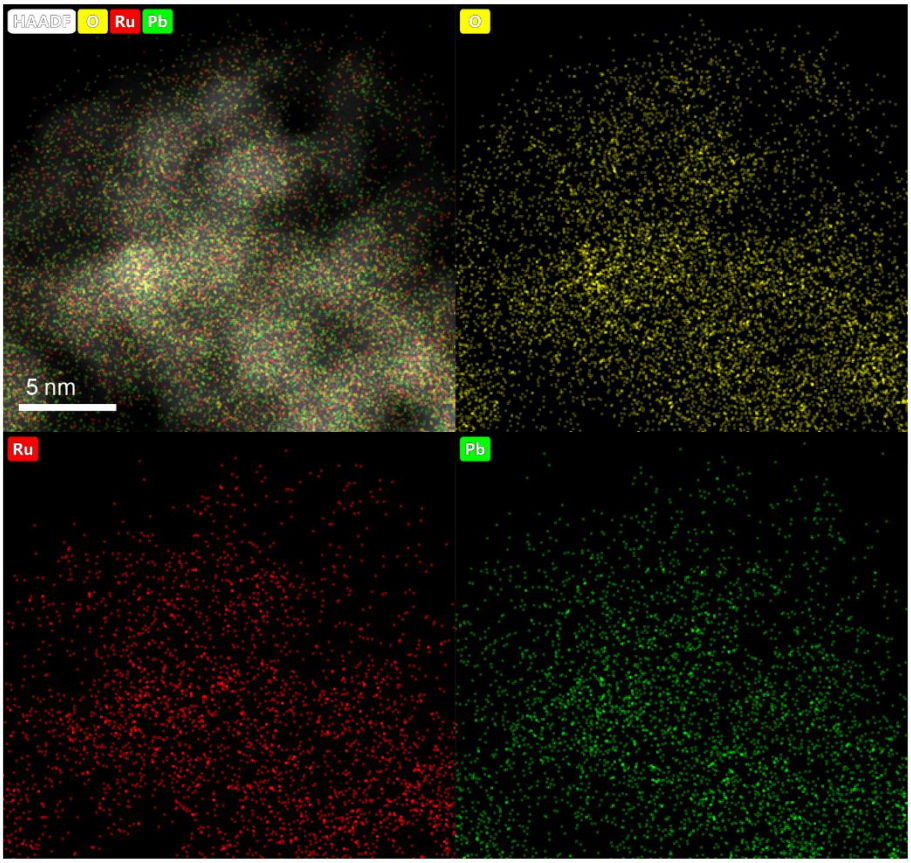

Figure S6. EDS mapping images of Ru_3PbOx nanoparticles under high resolution showing a uniform distribution of Ru and Pd metals.

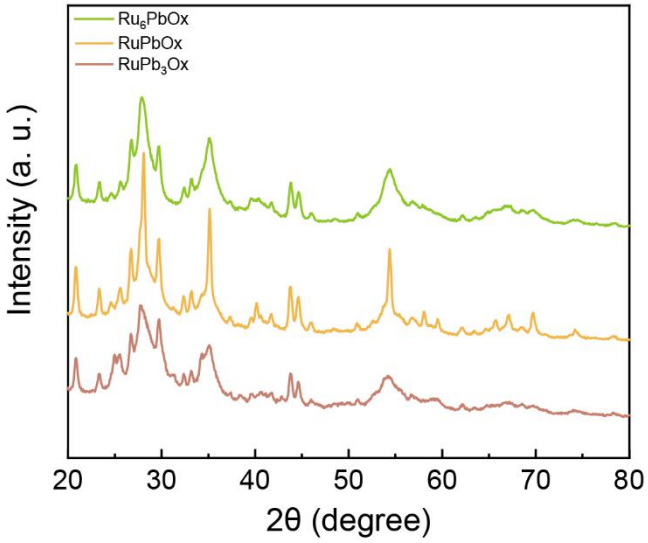

Figure S7. XRD patterns of different ratio of Ru-Pb oxide nanoparticles, including Ru_6PbOx, RuPbOx, and $RuPb_3Ox$.

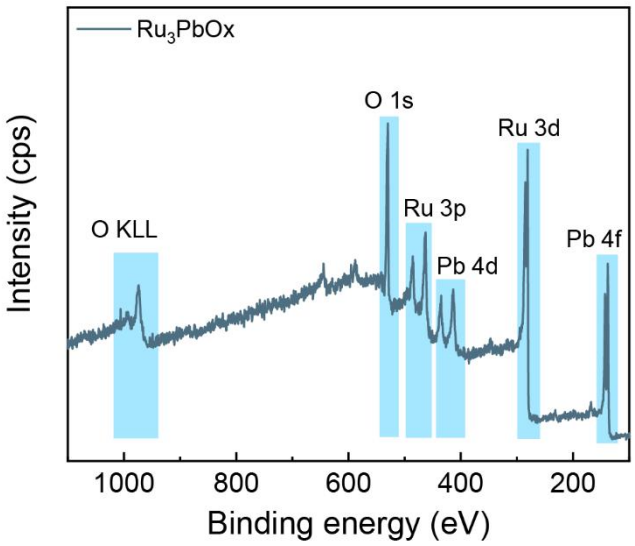

Figure S8. XPS survey spectra of Ru_3PbOx nanoparticles.

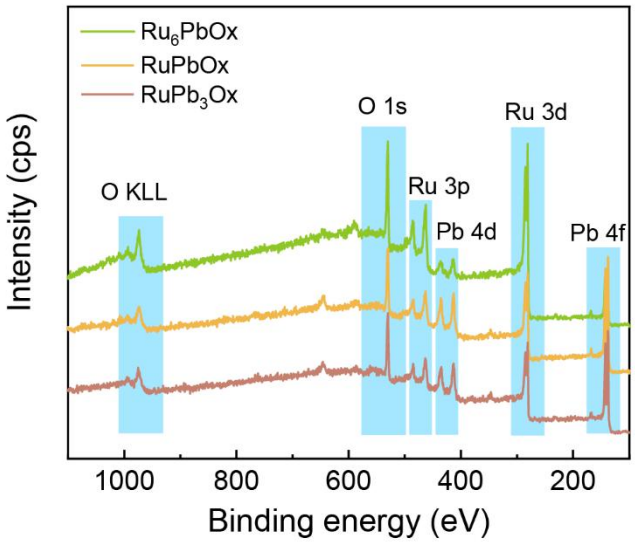

Figure S9. XPS survey spectra of different ratio of Ru-Pb oxide nanoparticles, including Ru_6PbOx, RuPbOx, and $RuPb_3Ox$.

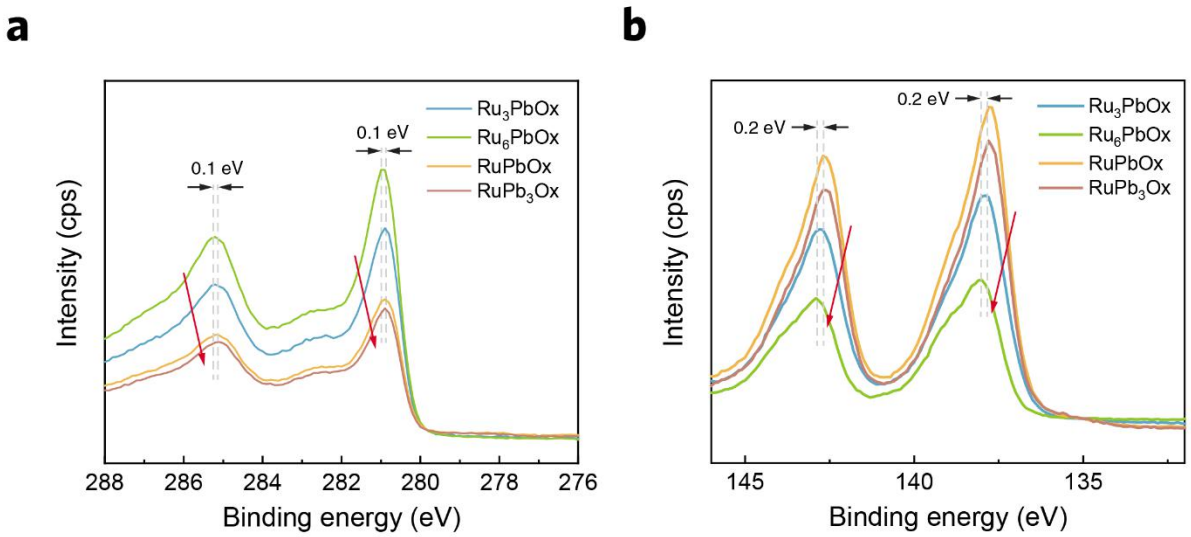

Figure S10. The comparison of high-resolution (a) Ru 3d and (b) Pb 4f XPS spectra of Ru-Pb oxide nanoparticles with different ratios, including Ru_3PbOx, Ru_6PbOx, RuPbOx, and $RuPb_3Ox$. Note that since Ru has a slightly higher electronegativity compared to Pb, the Ru would gain more electrons when the Pb content increases, leading to a shift toward metallic Ru^0. On the other hand, when the Ru content increases in the alloy oxide, the Pb would lose more electrons and lead to a shift toward Pb^+.

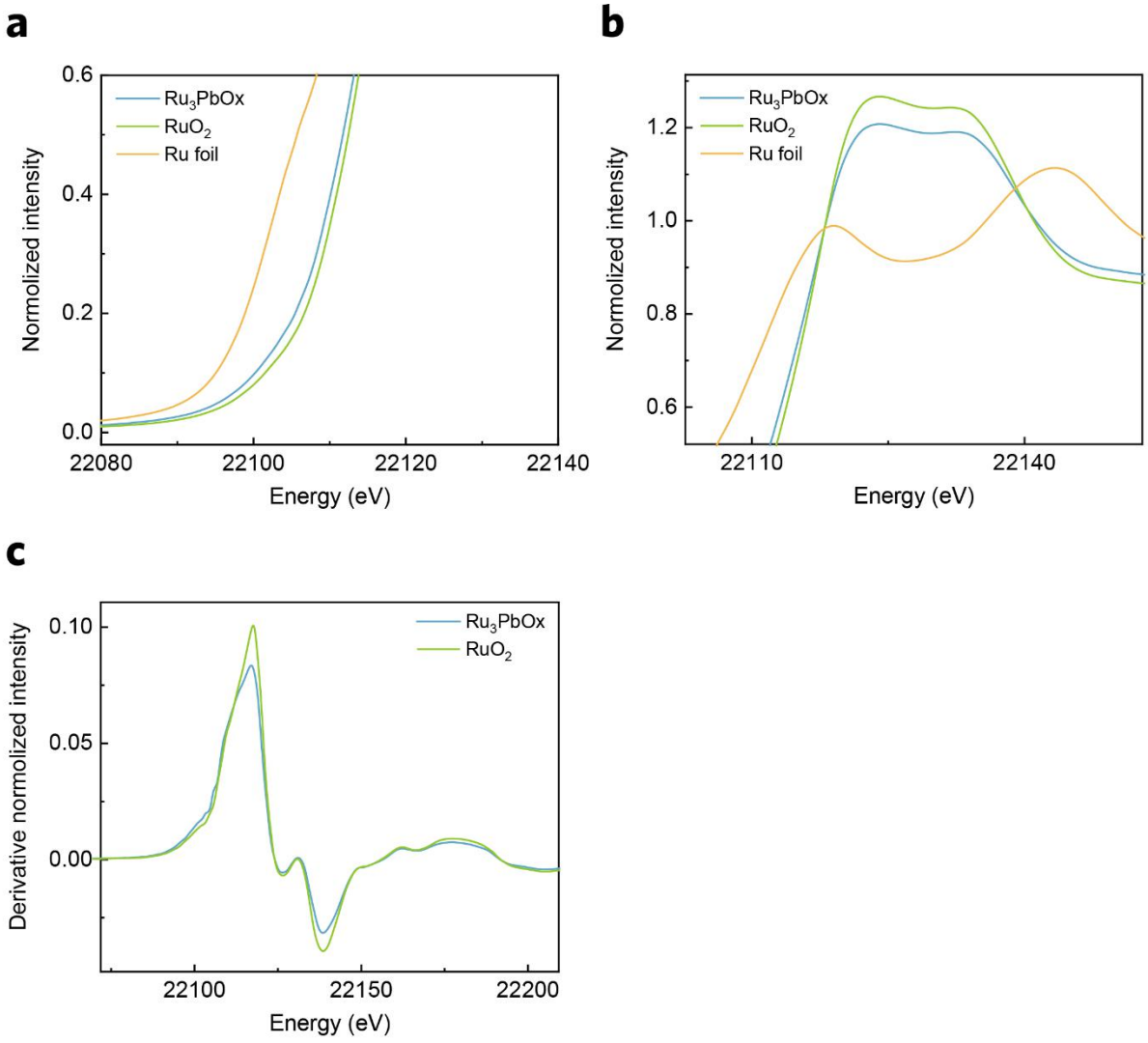

Figure S11. The zoom-in Ru K-edge XANES spectra of Ru_3PbOx, RuO_2, and Ru foil to show their differences in (a) oxidation states in rising edge and (b) white line. (c) First derivative of the normalized XANES of Ru_3PbOx and RuO_2 to demonstrate a small shift in rising edge.

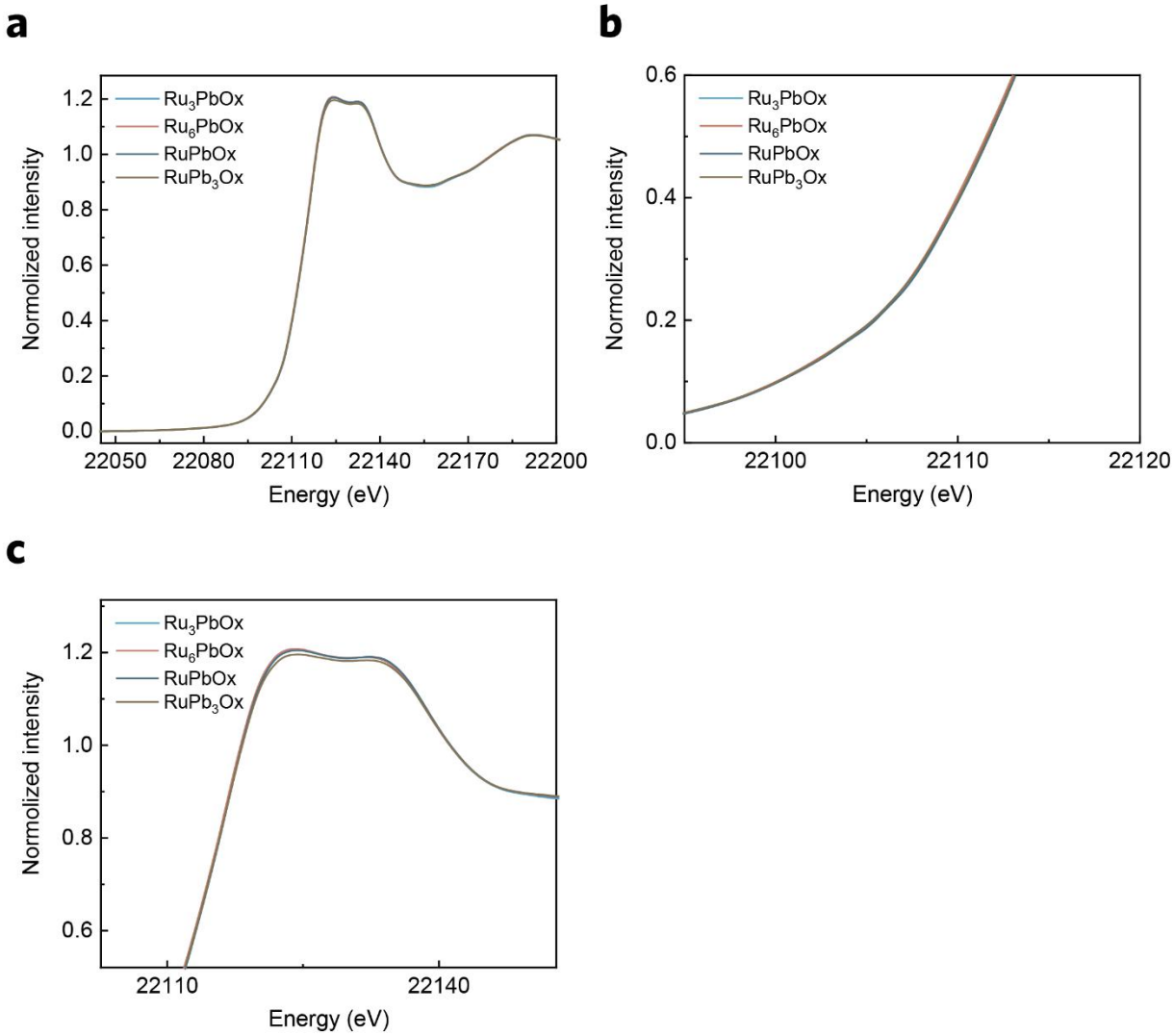

Figure S12. (a) The overall Ru K-edge XANES spectra, its zoom-in (b) rising edge and (c) white line of Ru-Pb oxide nanoparticles with different ratio, including Ru_3PbOx, Ru_6PbOx, RuPbOx, and $RuPb_3Ox$. This demonstrates the Ru oxidation states of different ratios of Ru-Pb oxide nanoparticle are nearly the same.

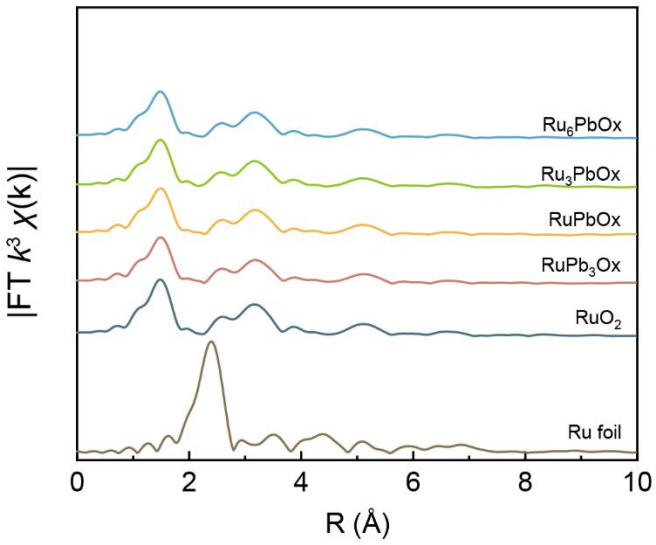

Figure S13. Ru K-edge FT-EXAFS spectra of Ru-Pb oxide nanoparticles with different ratio and the corresponding metal and metal oxide references. The Ru-Pb oxide nanoparticles show Ru−O peaks (1.50 Å) but no Ru−Ru peak (2.39 Å) [1].

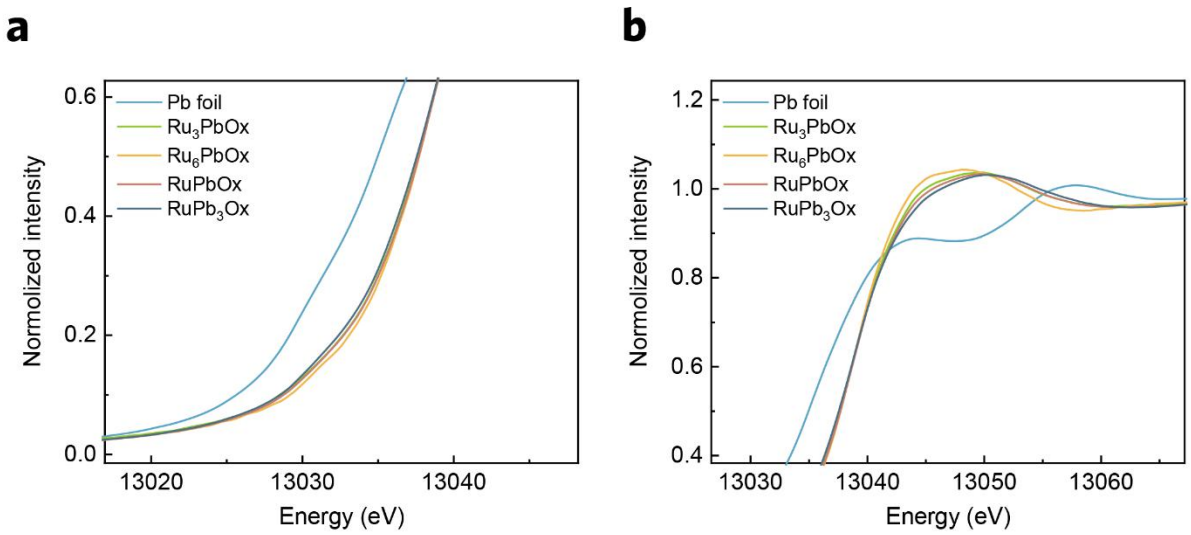

Figure S14. The zoom-in Pb L3-edge XANES spectra of Ru_3PbOx, Ru_6PbOx, RuPbOx, $RuPb_3Ox$, and the corresponding metal foil to show their (a) oxidation states in rising edge and (b) white line. This demonstrates the Pb oxidation states of different ratios of Ru-Pb oxide nanoparticle are similar and are distinct from the metallic Pb foil.

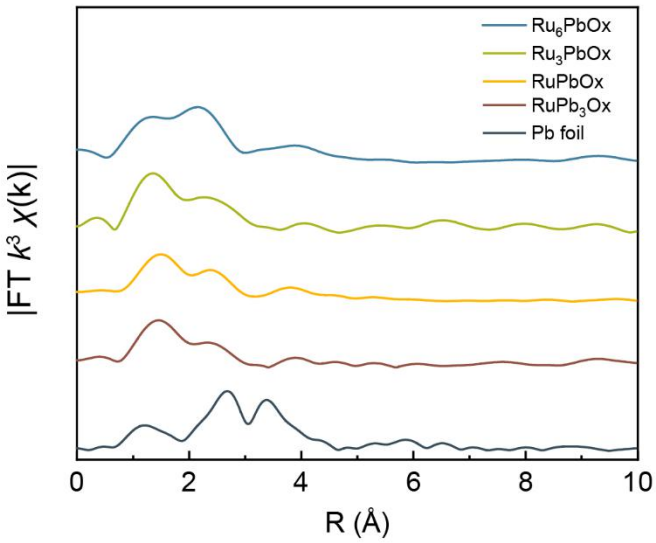

Figure S15. Pb L3-edge FT-EXAFS spectra of Ru-Pb oxide nanoparticles with different ratio and the corresponding references. The 2 peaks between 2−4 Å of Pb foil indicate the strongly structured amplitude and phase functions for Pb backscattering and is considered as the pattern of Pb−Pb bond [2]. The peaks between 1−2 Å of the different Ru-Pb oxide nanoparticles are the pattern of Pb−O bond [3].

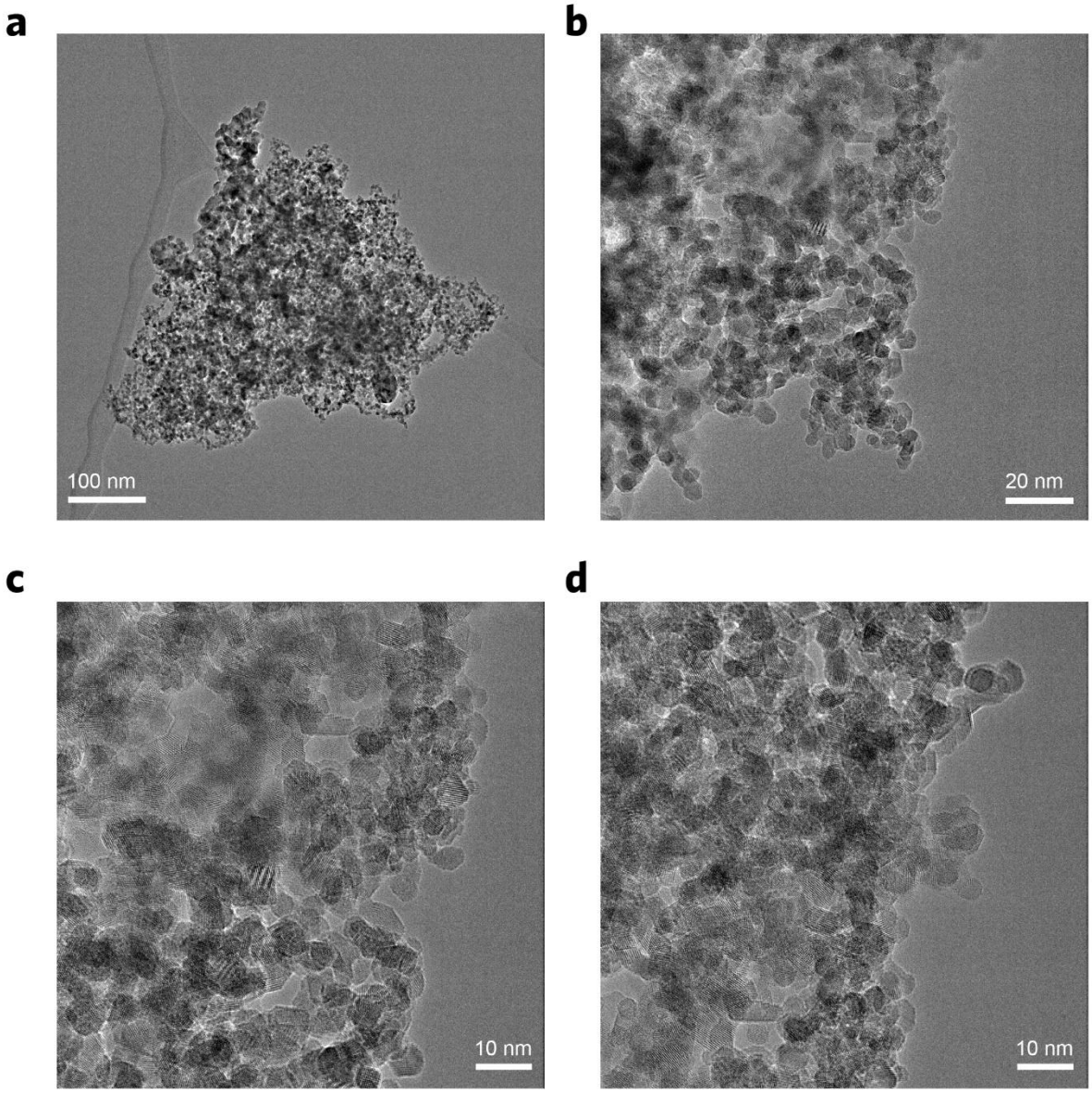

Figure S16. (a-d) TEM and HRTEM images of RuO_2 nanoparticles using an FEI Titan Themis aberration-corrected TEM.

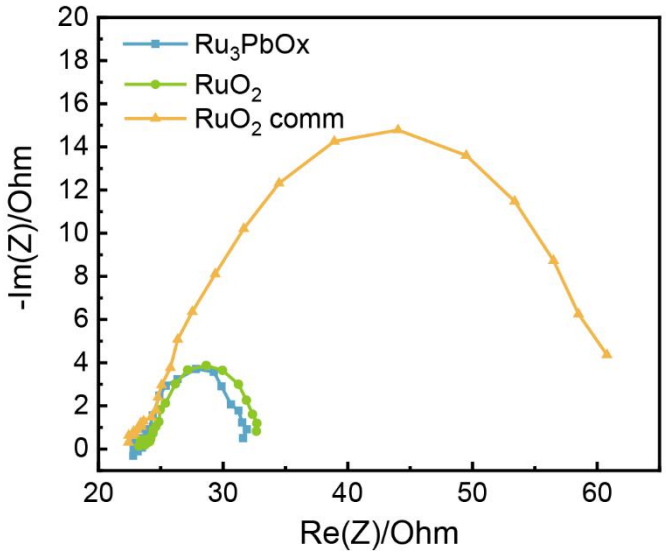

Figure S17. EIS plots of Ru_3PbOx, RuO_2, and commercial RuO_2. X-axis Re(Z) indicates the real part and Y-axis −Im(Z) indicates the imaginary part.

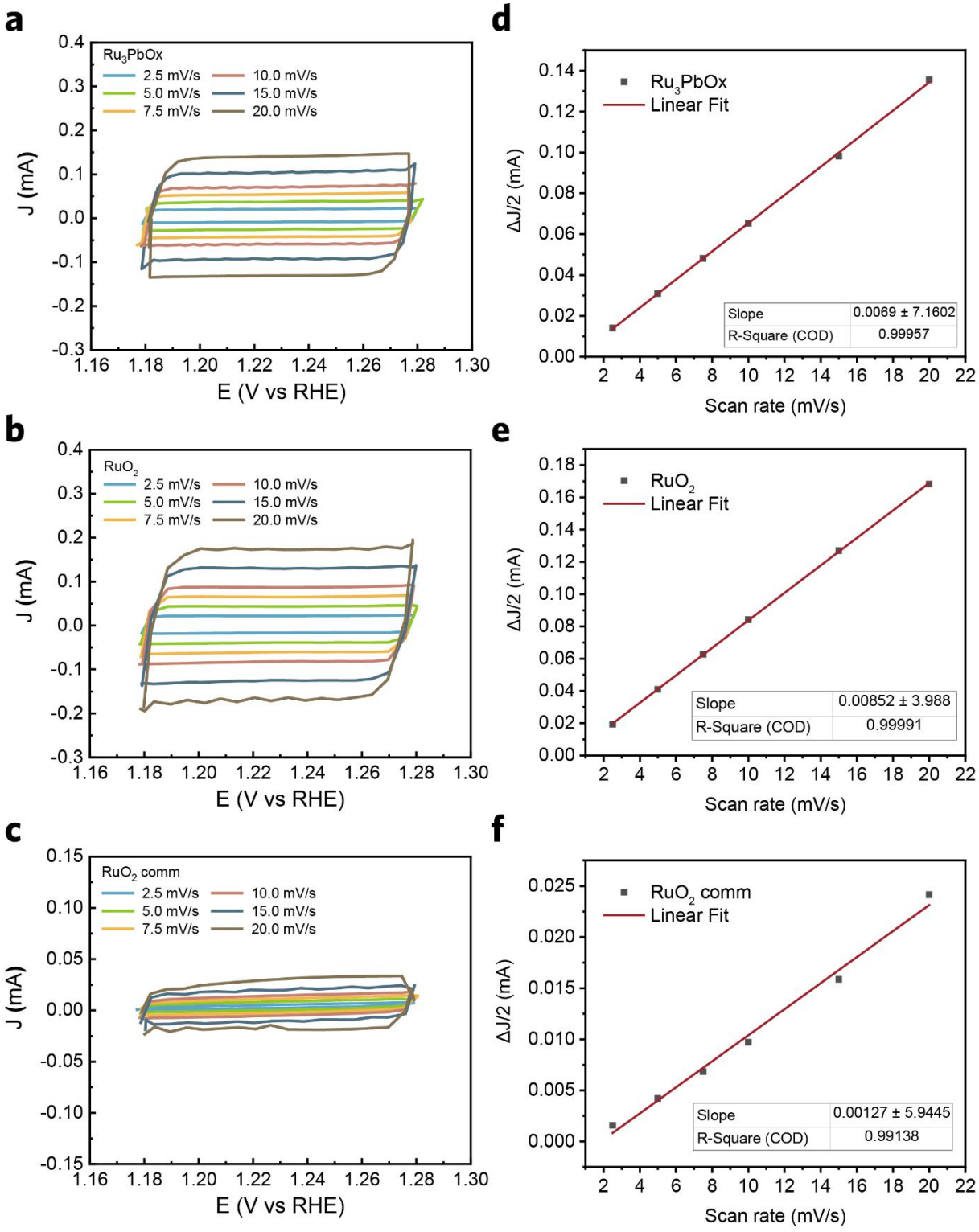

Figure S18. Cyclic voltammograms (CV) scan rate-current relationship and the corresponding Electrochemical active surface area (ECSA) analysis of (a, d) Ru_3PbOx, (b, e) RuO_2, and (c, f) commercial RuO_2. Details are demonstrated in Supplementary Table 3.

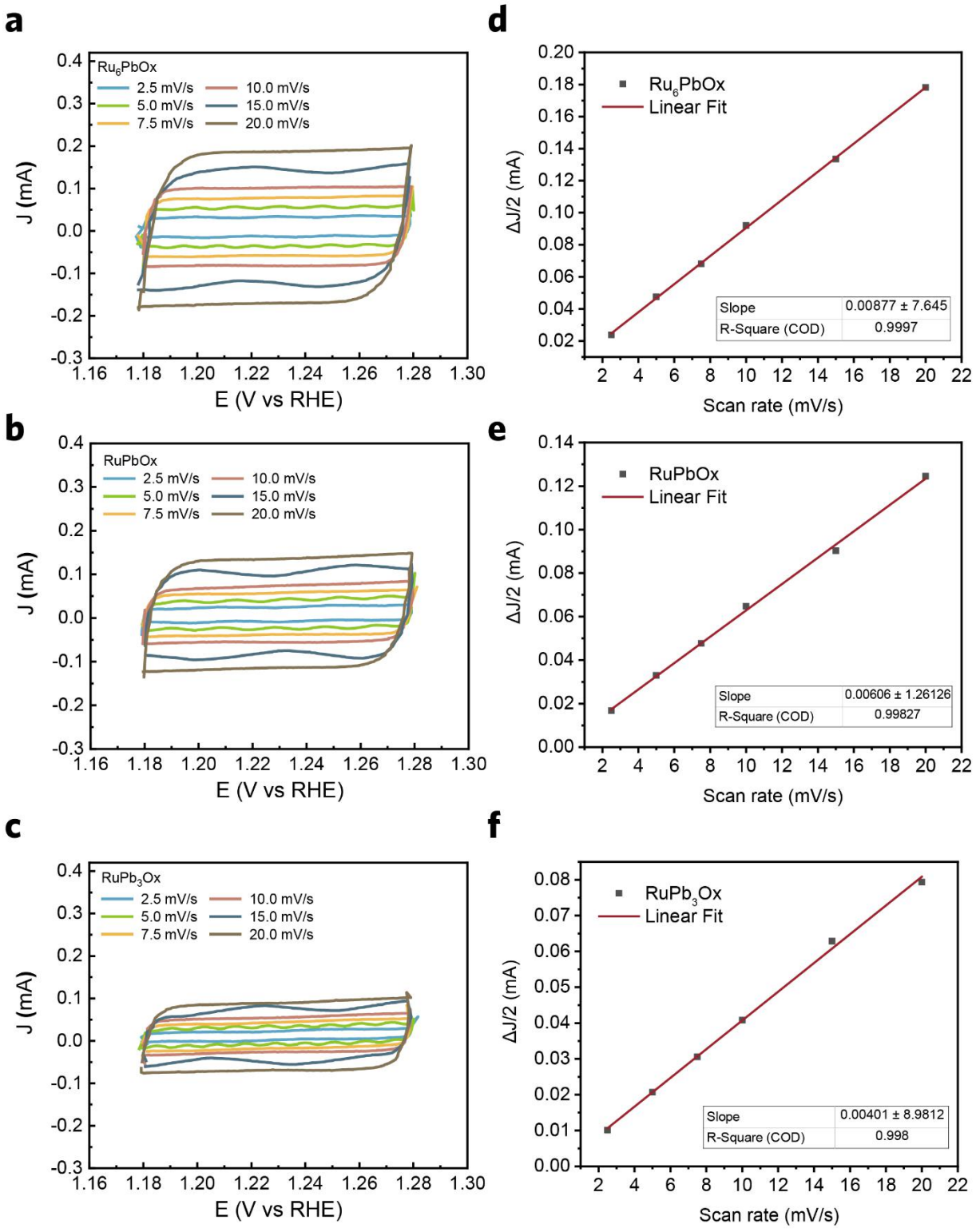

Figure S19. Cyclic voltammograms (CV) scan rate-current relationship and the corresponding Electrochemical active surface area (ECSA) analysis of (a, d) Ru_6PbOx, (b, e) RuPbOx, and (c, f) commercial $RuPb_3Ox$. Details are demonstrated in Supplementary Table 3.

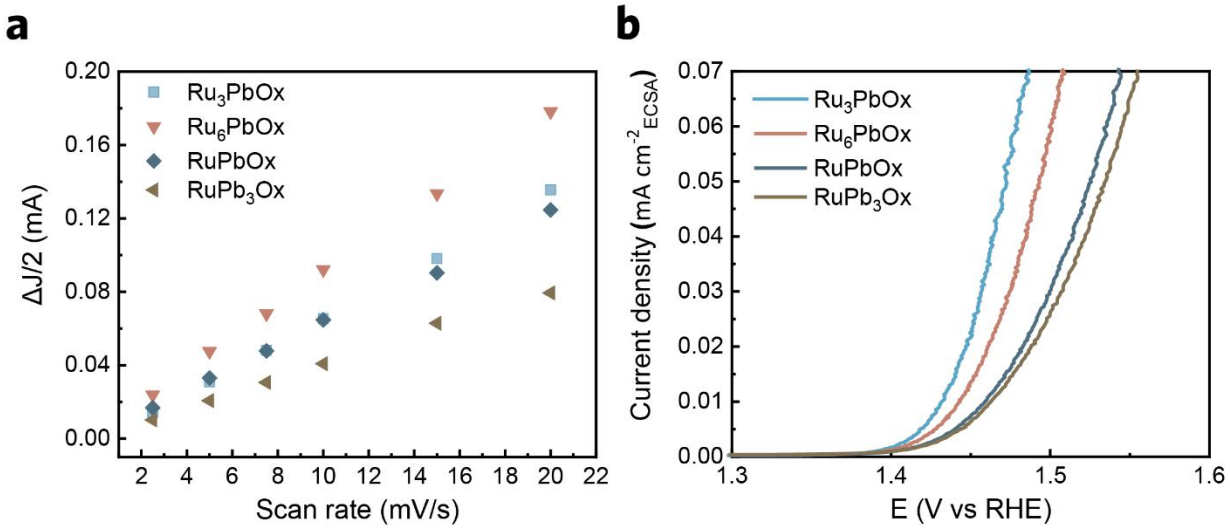

Figure S20. C_{dl} plots (a) for ECSA analysis derived from CV curves in Fig. S18 in the ESM and ECSA-corrected LSVs (b) of Ru-Pb oxide nanoparticles with different ratio, including Ru_3PbOx, Ru_6PbOx, RuPbOx, and $RuPb_3Ox$, showing Ru_3PbOx has the best intrinsic activity.

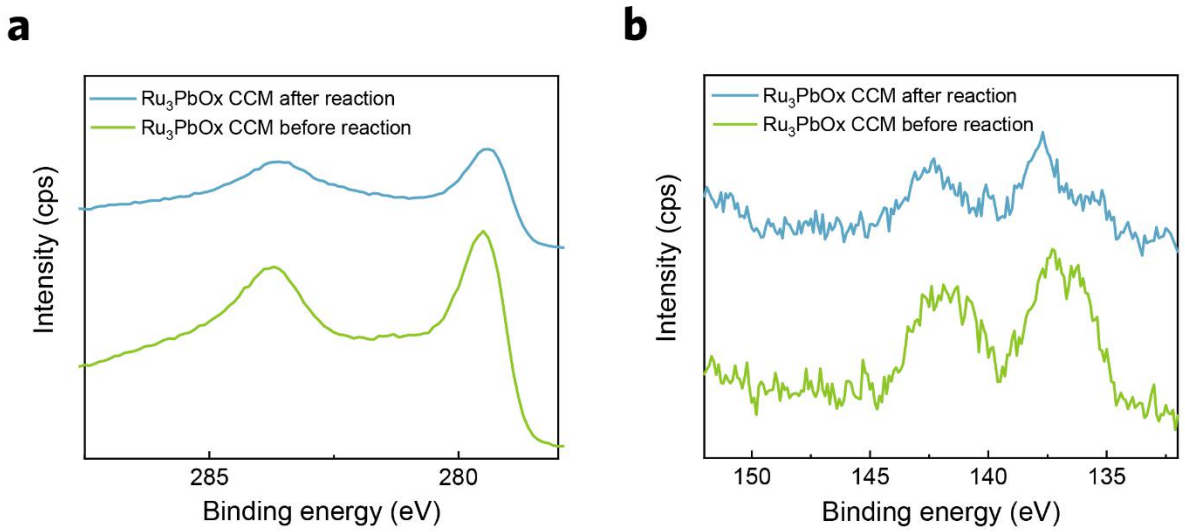

Figure S21. The comparison of high-resolution (a) Ru 3d and (b) Pb 4f XPS spectra of Ru_3PbOx CCM before reaction and after the 300 h stability test in PEM-WE in Fig. 4c.

Table S1. Surface elemental ratio based on XPS spectra. The values represent atomic ratio (at. %). RSF: relative sensitivity factor.

	Ru (Based on Ru3d, RSF 4.529)	Pd (Based on Pd4f, RSF 9.000)
Ru_6PbOx	85.11%	14.89%
Ru_3PbOx	72.62%	27.38%
RuPbOx	56.82%	43.18%
$RuPb_3Ox$	55.49%	44.51%

Table S2. EDS mapping elemental ratio of Ru_3PbOx.

Z	Element	Family	Atomic fraction
44	Cu	M	76.1%
82	Ru	M	23.9%

Table S3. OER overpotential at 10 mA cm^{-2} of different catalysts reported in this study. The test is based on the LSV scan on RDE.

	Overpotential (mV)
Ru_3PbOx	201
RuO_2	215
RuO_2 comm	298
Ru_6PbOx	208
RuPbOx	233
$RuPb_3Ox$	252

Table S4. ECSA analysis results of Ru_3PbOx, RuO_2, commercial RuO_2, and other different ratios of Ru-Pb nanoparticles. Slopes are calculated based on the scan rate-current relationship and their linear fitting. The ECSA was determined by: $ECSA = C_{dl}/C_s$, where C_{dl} is the double layer capacitance and C_s is the specific capacitance of the sample. In this study, a general specific capacitance of $C_s = 0.035\ mF\ cm^{-2}$ was used based on typical reported values [4]. C_{dl} was determined by the equation: $C_{dl} = i_c/v$, where i_c is the charging current and v is the scan rate. The C_{dl} was obtained from the slopes of the linear fitting in Figs. S18 and S19 in the ESM.

	C_{dl} (F)	ECSA (cm^2)	Roughness factor (RF)
Ru_3PbOx	0.0069	197.1429	2790.4155
RuO_2	0.00852	243.4286	3445.5566
RuO_2 comm	0.00127	36.28571	513.59822
Ru_6PbOx	0.00877	250.5714	3546.6586
RuPbOx	0.00606	173.1429	2450.7128
$RuPb_3Ox$	0.00401	114.5714	1621.6763

References

[1] Wu, Z.-Y.;Chen, F.-Y.;Li, B.;Yu, S.-W.;Finfrock, Y. Z.;Meira, D. M.;Yan, Q.-Q.;Zhu, P.;Chen, M.-X.;Song, T.-W.;Yin, Z.;Liang, H.-W.;Zhang, S.;Wang, G.; Wang, H. Non-iridium-based electrocatalyst for durable acidic oxygen evolution reaction in proton exchange membrane water electrolysis. *Nat. Mater.* **2023**, *22*, 100–108.

[2] Yu, Y. H.;Tyliszczak, T.; Hitchcock, A. P. Pb L3 EXAFS and near-edge studies of lead metal and lead oxides. *J. Phys. Chem. Solids* **1990**, *51*, 445–451.

[3] Zeng, L.;Huang, X.;Le, Y.;Zhou, X.;Zheng, W.;Brabec, C. J.;Qiao, X.;Guo, F.;Fan, X.; Dong, G. Reversible Growth of Halide Perovskites via Lead Oxide Hydroxide Nitrates Anchored Zeolitic Imidazolate Frameworks for Information Encryption and Decryption. *ACS Nano* **2023**, *17*, 4483–4494.

[4] Lin, Y.;Tian, Z.;Zhang, L.;Ma, J.;Jiang, Z.;Deibert, B. J.;Ge, R.; Chen, L. Chromium-ruthenium oxide solid solution electrocatalyst for highly efficient oxygen evolution reaction in acidic media. *Nat. Commun.* **2019**, *10*, 162.